Microstructural Deformation Mechanisms and Optimization of Selectively Laser Melted 316L Steel

Matthew J. Moneghan

Thesis submitted to the faculty of the Virginia Polytechnic Institute and State University

in partial fulfillment of the requirements for the degree of

Master of Science

In

Materials Science Engineering

Reza Mirzaeifar, Chair

Christopher B. Williams

Robert L. West

December 4, 2019

Blacksburg Virginia

Keywords: 3D Printing; 3D Printing Metals; Alloys; Additive Manufacturing; Microstructure; Strength; Toughness; Microstructure; Defect Tolerance

Deformation Mechanisms and Defect Tolerance in the Microstructure of 3D Printed Alloys

Matthew Moneghan

ABSTRACT

In this paper, a novel approach is utilized to investigate the deformation mechanisms at the microstructural level in 3D printed alloys. The complex in-situ heat treatments during 3D printing leaves a unique and complicated microstructure in the as-built 3D printed metals, particularly alloys. The microstructure is made of a hierarchical stacking of some interconnected geometrical shapes, namely meltpools, grains, and cells. These are connected to each other by boundaries that might have different element compositions, and consequently, material properties, compared to the interior region of each geometrical unit. Deformation mechanisms in this microstructure are still highly unexplored, mainly because of the challenges on the way of performing experiments at the micrometer length scale. In this work, we establish an image processing framework that directly converts the SEM images taken from the microstructure of 3D printed 316L stainless steel alloys into CAD models. The model of the complicated microstructure is then scaled up, and the scaled model is 3D printed using polymeric materials. For 3D printing these samples, two polymers with contrasting mechanical properties are used. Distribution of these two polymers mimics the arrangement of soft and stiff regions in the

microstructure of 3D printed alloys. These representative samples are subjected to mechanical loads and digital image correlation is utilized to investigate the deformation mechanisms, particularly the delocalization of stress concentration and also the crack propagation, at the microstructural level of 3D printed metals. Besides experiments, computational modeling using finite element method is also performed to study the same deformation mechanisms at the microstructure of 3D printed 316L stainless steel. Our results show that the hierarchical arrangement of stiff and soft phases in 3D printed alloys delocalizes the stress concentration and has the potential to make microstructures with significantly improved damage tolerance capabilities.

Deformation Mechanisms and Defect Tolerance in the Microstructure of 3D Printed Alloys

Matthew Moneghan

GENERAL AUDIENCE ABSTRACT

Many researchers have studied the impacts of laser parameters on the bulk material properties of SLM printed parts; few if any have studied how these parts break at a microstructural level. In this work we show how SLM printed parts with complex microstructures including grains, meltpools, and cells, deform and break. The cellular network that occurs in some SLM printed parts leads to a multi-material hierarchical structure, with a stiff network of thin boundaries, and a bulk "matrix" of soft cell material. This leads to similar properties as some composites, whereby the stiff network of cell boundaries leads to increased damage tolerance. We show both computationally through finite element analysis, and experimentally through multi-material 3D fabrication, that the microstructure leads to increased crack length in failure, as well as lower toughness loss and strength loss in the event of a crack. Essentially, the complex nature of the formation of these parts (high heating and cooling rates from laser melting) leads to a beneficial microstructure for damage tolerance that has not been studied from this perspective before.

Attributions

The following people helped collaborate in this work and co-author these papers:

Reza Mirzaeifar – Assistant Professor at Virginia Tech, Department of Mechanical Engineering

Christopher Williams – Professor at Virginia Tech, Department of Mechanical Engineering

Lindsey Bezek – Graduate student at Virginia Tech, Department of Mechanical Engineering

Logan Bass – Graduate student at Virginia Tech, Department of Mechanical Engineering

Their specific contributions are the following:

Chapter 1: Reza Mirzaeifar helped plan the experiments. Reza Mirzaeifar, Lindsey Bezek, and Logan Bass helped prepare the paper for publication. The samples used for experimentation were printed by Lindsey Bezek and Logan Bass through the use of Christopher Williams voxel-based printing.

Chapter 2: Reza Mirzaeifar helped prepare the paper for publication.

Table of Contents

INTRODUCTION

Industries all across the globe use different manufacturing methods to create parts for their respective purposes. Some of these industries require high-performance parts, often leading to material selection involving some combination of properties including high ultimate strength, high toughness, high hardness, or high damage tolerance. In addition to down selecting materials in order to get the best properties, industries such as the aerospace, automotive, and biomedical industries also have complex geometries to accomplish a given task. These parts can be challenging, costly, or even impossible to subtractively manufacture through traditional means such as milling, turning, or stamping. Some of these parts can be created through techniques such as forging or casting, but this limits material selection to an often worse grade of material. One recent method of part production that has grown drastically within the last decade is the use of a 3D fabrication technique called Selective Laser Melting. This involves a bed of powder and a build chamber, whereby a fine layer of powder is deposited into the build chamber, then the laser melts a cross-section of the fabricated part at that height. Another layer of powder is deposited and the process repeats until the part is fully created.

This is a simple process from a description standpoint, but there are deep complexities in the heating and cooling mechanisms that govern how the part is formed. The heating and cooling rates are in the range of 10^5-10^8 kelvins per second; this leads to a complex hierarchical microstructure formation. The microstructure of these parts is threefold: grains as most metals have which are just clusters of similarly oriented crystalline structure. Secondarily there are meltpools, which are semi-circular extrusions of material that form from the solidification of the

molten material as the laser scans. Lastly, there is a network of cellular structures and boundaries on a much smaller scale than the other two structures. Grains and meltpools occur on the order of 10-100 μm, whereas the cells occur on the order of 1-5 μm with boundaries as fine as 0.1 μm.

Many researchers have studied the influence of the processing parameters of the laser: laser power, scanning speed, hatch spacing, and the layer thickness, on the resultant part's bulk properties such as yield strength, ultimate strength, toughness, elastic modulus, and hardness. Until this point, no one has studied the fundamental mechanisms behind the failure mode of these parts. More specifically, how the strain field of the parts is distributed across the body, and how a crack propagates when considering the meltpools and the cellular network. In the first paper of this thesis, we show just this. In the paper, we discuss how the strain is distributed across the body of an SLM part, specifically at the three types of meltpool boundaries, and an area far away from any boundary. In addition, we show that the hierarchical structure that develops from the formation of SLM parts leads to a damage-tolerant body, losing less strength and toughness when cracked or fractured than a solid phase bulk material.

In the second work, we show that this cellular network that forms has a multitude of shapes and sizes possible. A "standard" cell of each type is measured, one for the inner granular cells far away from any boundary, one for the epitaxial cells that form at layer-layer meltpool boundaries, and one for the non-epitaxial cells that form at track-track meltpool boundaries. These cells were then adjusted within a reasonable design space of formation (approximately 15% of their nominal value). A range of simulations was run, encompassing all influential combinations of these cells' parameters. These were all tested to failure in finite element analysis, and the

resultant toughness and maximum stress of each body was measured. These values were then compared both against the other values within that cell and also to the other cells and loading conditions. These are presented together in one large table showing the best and worst result of each type of cell in each loading condition for strength and toughness. In addition, the individual studies are shown through contour plots showing three input variables at a time and the output parameter as a color.

Deformation Mechanisms and Defect Tolerance in the Microstructure of 3D Printed Alloys

1 Introduction

In response to the opportunities and challenges of the 21st century, Additive Manufacturing (AM) is rapidly replacing the conventional manufacturing methods. After years of extensive development in AM methods for polymeric systems, 3D printing of metals, particularly by the Selective Laser Melting (SLM) technique, is now being extensively adopted by multiple industry subsectors. Investigating different aspects of the mechanical properties of SLM parts has been attracting growing attention in the past few years [1-13]. Parts printed in this manner have many advantages over traditionally manufactured parts, including graded material compositions, complex geometries that are unobtainable through subtractive manufacturing, and less material usage [14]. These parts are currently in use across multiple fields such as the automotive industry in performance vehicles, the aerospace industry as manifolds and rocket engines, and the medical field as joint replacements and prosthetics [15-17]. As these parts are produced more for research and commercial use, more studies are occurring on the complex substructures of the materials. Compared to polycrystalline metals, in which grains are the major microstructural feature of the material, SML parts have two unique extra microstructures: cells and meltpools. Meltpools are roughly semi-circular shapes that form as the laser melts a section of the powder, and then solidifies [18-20]. These meltpools lead to an anisotropy at the macro scale due to their geometry [21]. The materials are often stronger in the plane of printing rather than in the build direction due to a mechanism similar to delamination within polymeric AM materials. Due to the extreme

heating and cooling rates during the solidification process, complex sub-structures are formed inside the meltpools, which are known as cells [3, 22-25]. Cells are a sub-granular structure (0.5 to 3 micrometers) that are generally shaped like an elongated hexagon. These cells also have finite thickness boundaries between them that have been shown to have different compositions of materials. In the case of 316L stainless steel, the cell boundaries have been shown to have higher concentrations of chromium, nickel, silicon, and molybdenum, but the exact percentages of each, and the phase of this material is disputed [26-28].

In this field, researchers have studied the impacts of processing parameters on the macro properties of the parts produced. The impacts of laser power and scan speed on the grain structure has been studied [29]. Another work shows an optimization of laser power, scan speed, and hatch spacing in order to increase the yield and tensile strength of the studied steel (4130) [30]. Aboulkhair et al. show the impacts of laser power, scan speed, hatch spacing and layer thickness for different aluminum alloys for optimal densities [31]. While these and many other research works have studied the impact of processing parameters on the macrostructure of AM alloys and their mechanical properties at the macro scale, few if any have studied the deformation mechanisms of the cellular structures seen in AM parts [32]. If these mechanisms can be understood and quantified, then the microstructural properties and geometries can be optimized in order to fabricate stronger parts from a given material.

In this paper, we study the deformation mechanisms at the microstructural level, at the vicinity of cells and meltpool boundaries. Deformation mechanisms at this scale directly govern the bulk mechanical properties, particularly the damage tolerance of the AM material, at the macro scale. A finite element framework is utilized to investigate the stress and strain distributions at the microstructural level and the interconnection between these distributions and the macroscopic

material properties. A novel framework is developed and utilized for experimentally investigating the deformation mechanisms at the scale of cells and meltpools. In this research, 316L stainless steel is selected as a representative model alloy system to understand the basic principles of deformation mechanisms. Other alloys such as Al-Si, Co-Cr-Mo [33], and AlSi10Mg [34] show similar cellular structures, but 316L is a widely studied and used material and therefore was deemed appropriate for this study.

2 Methods

2.1 Framework

In both the experimental and computational frameworks, the studied microstructures are direct copies of segments of a real SLM sample viewed under SEM. These models were reproduced and turned into a segmented image through a trained neural network. There were multiple challenges in studying the deformation mechanisms at the micro-scale in these materials, which arise from the size of cells. We targeted using digital image correlation (DIC) [35] to track the strain distributions of the complicated microstructure of AM alloys. However, tracking the strain field at the vicinity of cells, and cell boundaries (which are features as small as 100 nanometers wide) by using DIC requires multiple visible “speckles” across each feature, which is extraordinarily difficult. We overcame this hurdle through an innovative solution; in this method, we printed a duplicate of the microstructure of SLM alloys by scaling the size upwards and used a multi-material polymeric 3D printer. In the 3D printed polymeric part, we used an analogous stiff and flexible material as representative materials to replace the cell boundaries and cells respectively. This solution allowed for a much higher resolution strain field from actual experimentation. The materials we chose to use have exaggerated characteristics with respect to what the cells and boundaries are currently thought to be; in this case, the cells are a more ductile

material with higher elongation and lower strength, and the cell boundaries are a higher strength material that is stiffer with a lower elongation [26-28]. With this method, the exaggerated properties allow the strain field to be easily seen as the materials have a much higher differential between their properties than the real materials. It is worth noting that although we did not use the same materials as the SLM alloys, duplicating the exact microstructure and also following the trend of difference between the cell and cell boundary materials, gave us many unexplored details of the deformation mechanisms at the microstructural scale of AM alloys. The validity of these findings is approved by our computational investigations and is discussed in the following sections.

In addition to the scaled-up experiments, we performed FEM simulations of the geometries represented by considering a more realistic choice of hard and stiff metals for the cell boundaries and cells. The two representative materials were 316L for the cell as we represented 316L bulk AM metal, and a modified 4340 for the cell boundary in order to mimic the higher concentrations of chromium, nickel, silicon, and molybdenum in cell boundaries, as observed in the experiments [26-28]. The boundary material was modified such that the elastic region was unchanged, but the plastic region was extended such that this representative material has the same toughness as the 316L. These models had damage associated with them based on their yield and ultimate tensile strength values. Both the computational and experimental studies are utilized to investigate multiple unexplored fundamental aspects of the deformation mechanisms of the SLM alloys, and particularly to scrutinize the defect tolerance of the material with such a hierarchical microstructure. Our results show that the arrangement of stiff and soft material at the microstructure of SLM alloys, is inherently causing a remarkable resistance to the possible defects, and such a defect tolerance can be improved by engineering the microstructure.

2.2 Image Processing

Accurate images from the microstructure were needed to perform both the experiments and the FEM simulations. For each simulation or experiment, an SEM image was to be processed for creating either the finite element model or a CAD model for 3D printing the microstructure duplicates. In order to skip processing all the SEM images by hand, we used UNet, which is a neural networking software that allows images to be segmented into sections based on a relatively low number of training images. UNet has been used in the biomedical field for automatically identifying features in images such as lesions in livers [36], vertebrae [37], and internal organs [38]. To the best of our knowledge, UNet has not been used for processing optical or electron microscopy images of metals and their microstructures before this work. In this paper, we implemented this method to transfer SEM images into both finite element models and CAD files. We specifically focused on a segmented image where the cell boundaries are separated from the cells. This is a challenge to do manually, as a properly scaled image contains around 4 meltpools, and there are approximately 700 cells per meltpool thus the image will roughly contain 2800 individual cells. For that reason, only a small set was done by hand (8 images) as a training set, and then transformed and modified to get a slightly extended set of 32 images. The training set was able to train UNet to produce accurate (<30% loss) images up to 512×512 pixels. Two examples of SEM images and their UNet segmented counterparts are shown in Figure 1. Using the trained neural network, grayscale SEM images are transferred into black and white images in which black color represents the cells, and white represents the cell boundaries. These images will be used for constructing the CAD and the finite element models, as discussed in the following sections.

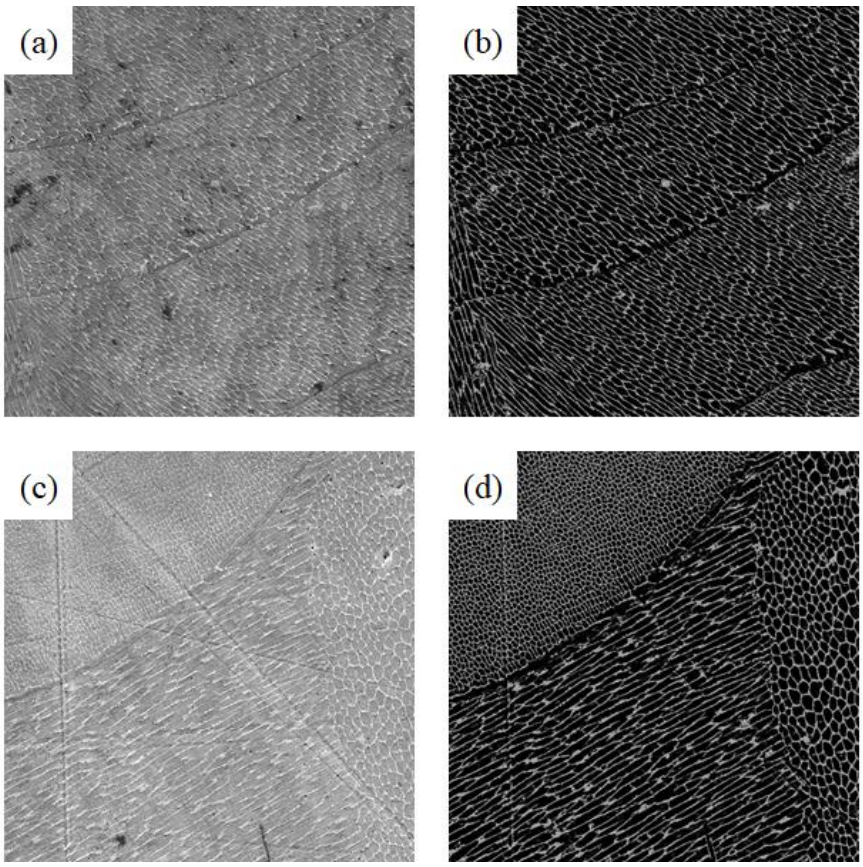

Figure 1: (a) and (c): Raw SEM images from the meltpools and cellular structures. (b) and (d): UNet post-processed and segmented images.

SEM images from a zoomed-out microstructure with a few meltpools were first put through UNet to extract four smaller sections (see Figure 2). These sections represent four main "features" of the microstructure upon which we are performing tests: the bulk cells inside a meltpool (Figure 2b), the layer-layer boundary which is the intersection of two meltpools in the print direction vertically, (Figure 2c), the track-track boundary which is the intersection of two meltpools in the printing plane horizontally, Figure 2d), and lastly the triple junction which is where a layer-layer boundary and a track-track boundary meet, (Figure 2e).

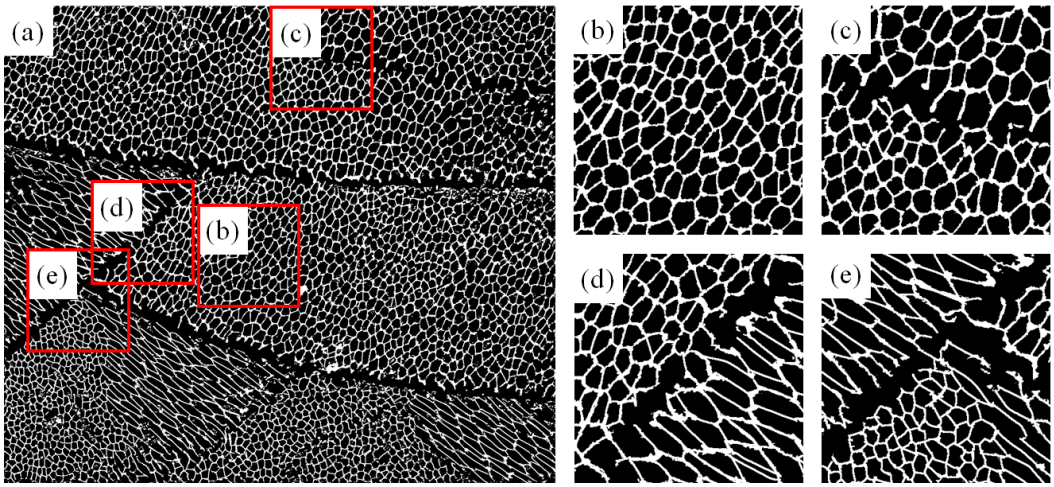

Figure 2: a) Segmented image of 5 meltpools and their respective cells and boundaries. (b) The inner granular section of cells chosen, (c) the Layer-Layer meltpool boundary, (d) the Track-Track meltpool boundary, and (e) the Triple junction boundary. The black and white colors correspond to the cell and cell boundaries, respectively.

2.3 3D Printing Representative Samples

To study the micro-scale deformation mechanics, each of the four extracted parts that represent the building blocks of an SLM steel part (Figure 2b-e) in addition to the full-scale image (Figure 2a) were fabricated using the material jetting AM process. In this process, a layer is formed by liquid photopolymer droplets being selectively jetted onto a substrate. After the material is deposited, a roller smooths the droplets, and a UV light cures the deposition. The substrate then moves downward to allocate space for the subsequent layer formation. The Stratasys Objet Connex350 was used for printing, and all of the images were printed at a 152×152 mm size with a thickness of 2 mm. The samples were printed with VeroWhitePlus and TangoBlackPlus for the cell boundaries and cells, respectively. VeroWhitePlus is a rigid, white material with an ultimate tensile strength of ~45 MPa, modulus of elasticity of ~744 MPa, and elongation of ~19% at failure. TangoBlackPlus is a rubber-like, black material with an ultimate tensile strength of

~0.39 MPa, modulus of elasticity of ~0.21 MPa, and elongation of ~180% at failure [39]. The difference in material properties is significant; thus, the strain field differences will be perceivable. The printed samples are shown in **Error! Reference source not found.**.

For conventional material jetting, single material assignments are given to each standard tessellation language (STL) file. In this case, we bypassed the generation of the STL file and instead used a custom algorithm to assign materials to each layer slice based on the image's grayscale shading. Through this voxel-based material assignment, a set of bitmap images represented the layer slices and each pixel of an image corresponding to an individual material droplet. This method provided an efficient way to directly manufacture multi-material parts corresponding to high-resolution grayscale images.

On the Connex350 system, a gel-like support material is used to encase all surfaces of printed parts, but the operator can select whether to have support material on top surface (matte finish) or not (glossy finish). Parts were printed in "glossy" mode, to leave the top surface clean. Following printing, the support material is removed with a high-pressure water jet station.

2.4 Digital Image Correlation (DIC) and Tensile Tests

DIC tests were performed on the 3D printed polymeric samples (which represent the microstructure and material distribution of an SLM printed alloy) to study the deformation mechanisms and the strain delocalization at different locations. Speckle patterns were spray-painted on one side of all the samples with a range of gray tones to assist the DIC. Ncorr [40] package was used for analyzing the images. The printed specimens were tested in an Instron 5984 Universal Testing Machine with an Instron 150 kN static load cell. The uniaxial tensile tests were performed by applying displacement boundary conditions. A displacement rate of 5

mm/min was selected in all the experiments to ensure the validity of quasi-static loading conditions.

These samples are non-isotropic, and thus need to be tested in both directions. With that in mind, 3 tests were performed for each of the 4 building block samples. First, they were strained to 2% in the horizontal direction, as will be called "aligned direction" in the following, since they are aligned with the layer-layer meltpool boundaries. Next, they were strained to 2% in the vertical direction (namely orthogonal direction). Lastly, a crack was added to the sample for studying the defect tolerance at the microstructural level. This crack had a specific geometry to try and get results as consistently as possible. The cracks added to any of the geometries in this paper are always $1/6^{th}$ the overall sample length, located at the center of a cell, and roughly in the center of the direction perpendicular to the crack. The priority of following those three rules was in that order respectively. As these samples were all the sections of the larger image, we knew that the pinnacle of these tests would be following the crack propagation of the large sample, and the result of testing in the direction of the build plane would lead to better results (rather than the delamination direction). For the full-size model, we wanted to have no prior damage having any influence on the results of the crack propagation test, and thus the cracked sample is only tested in the aligned direction.

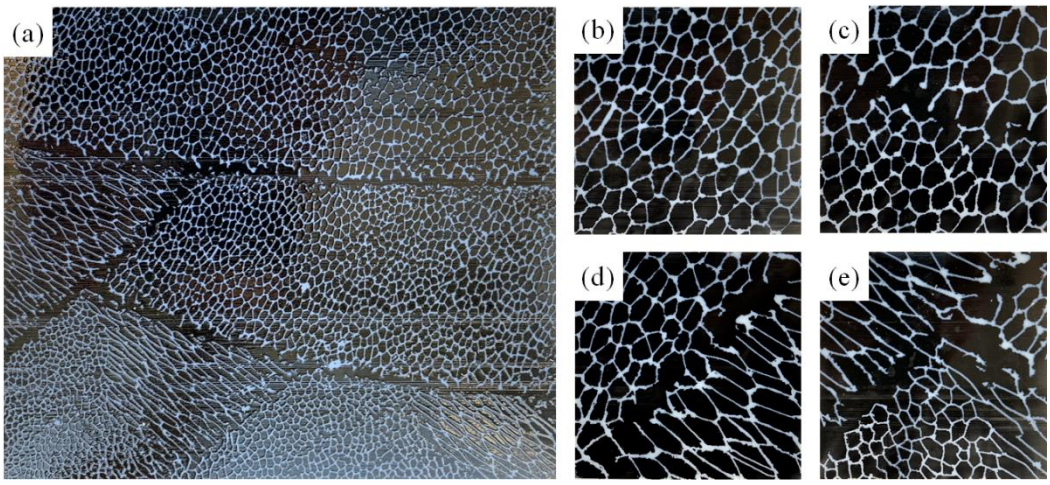

Figure 3: 3D printed representative samples using TangoBlackPlus (soft) and VeroWhitePlus (stiff) polymeric materials. The geometry follows the microstructure of an SLM sample. (a) Full sample with five meltpools, (b) the inner granular section of cells chosen, (c) the Layer-Layer boundary, (d) the Track-Track boundary, and (e) the Triple junction boundary.

2.5 Finite Element Modeling

For the FEM studies, a total of 5 unique geometries were used to test, with two sets of materials. For the case of samples made of 316L powder, the composition of the material inside the cells is very close to the original alloy. The cellular material is suspected to have a higher content of nickel, chromium, silicon, and molybdenum; in addition, it is suspected to have BCC phase on some specific cases [27]. For two reasons this boundary material is likely to be stiffer: the nickel, chromium, and molybdenum are all hardening and strengthening elements added to steel, and secondarily BCC materials generally form stiffer and stronger materials than FCC phase materials. For these reasons, representative steel that has a higher stiffness, and higher strength but lower elongation was chosen as a representative material for the cell boundaries. In this case, 4340 was used as a base material but modified to have an equivalent toughness compared to the

316L. The new material's plastic curve was extended along its normal path using a Ramberg Osgood curve fit such that the toughness was equal to 316L steel's toughness (see Figure 9e). These two materials were then used in the FEM with an additional complexity of adding ductile damage. In these simulations, the damage starts at the yield values respectively, and the material goes through linear softening in the damaged regime. The material reaches full failure at a tensile stress of its ultimate strength respectively.

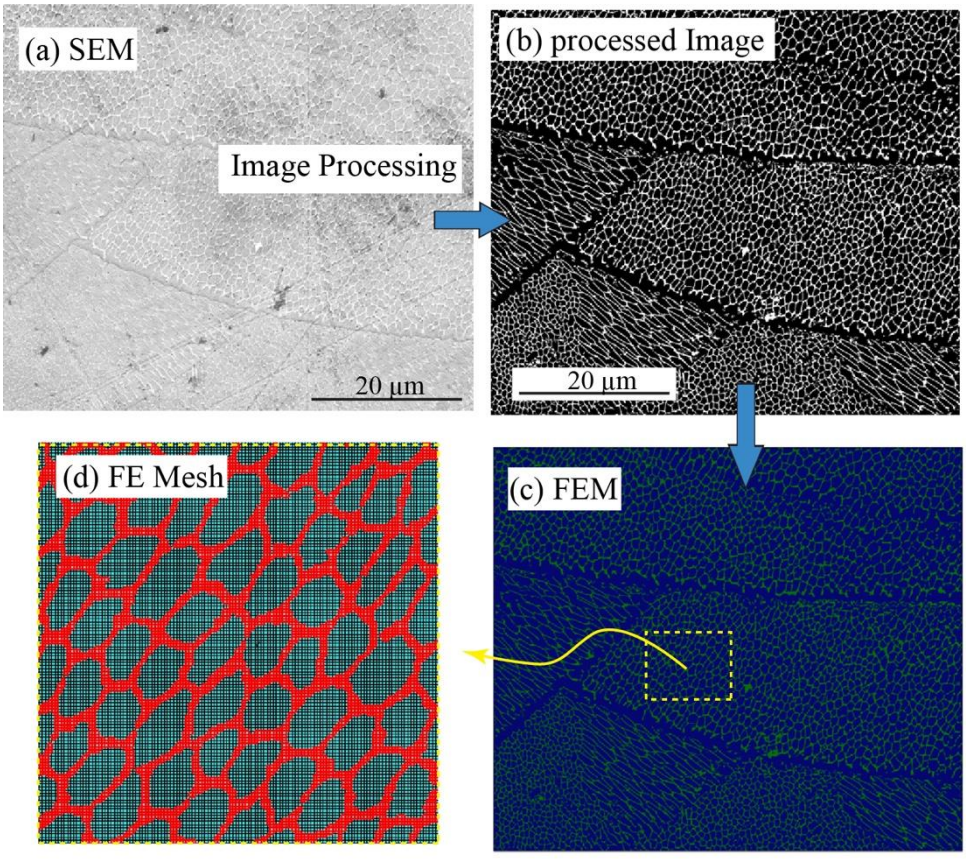

Figure 4: UNet transfers the SEM image of an SLM printed steel sample (a) to a processed image (b), which is then directly used to create a finite element mesh from the complicated microstructure. The material inside the cells (black) and at the cell boundaries (white) are detected in the processed image (b), and two different sets are created in the finite element model for these two materials (c and d).

For the FE simulations, a method of inputting the geometry (including cells and boundaries into the software from a picture) was created, as shown in Figure 4. A custom Python script was developed that is able to read the segmented image outputted from UNet and create two sets, one for cells and one for cell boundaries. A grid mesh was then created where one pixel is sized at one element. These sets were applied such that the set of cells had the 316L material applied to it, and the set of boundaries had the modified 4340 material applied to it. Boundary conditions were applied to model a uniaxial tensile test [41]. A monotonic displacement was applied to the unclamped edge of the sample to simulate a 20% strain in the loading direction such that the sample was strained to failure. In order to measure the force across the loaded edge, a coupling is used to tie that surface to a point which is rigidly fixed in the loading direction (U1 or U2 only depending on the model). This point can then be measured as a summation of the force across the entire face and is used in the stress strain calculations.

As for the meshing elements that create this model, the cells are the following elements in Abaqus. The elastic modulus was 189000 MPa, the Poison's ratio was 0.3, density was 7.89E-15, the plasticity is tabular every 10 MPa following the curve shown in FIGURE 9. The damage model was Ductile Damage within Abaqus, with the following parameters: Fracture strain of 0.410, Stress Triaxiality of 0, and Strain rate of 0, with linear softening, displacement based maximum degradation of 0.0164 at failure. The cell boundaries are the following elements in Abaqus. The elastic modulus was 207000 MPa, the Poison's ratio was 0.3, density was 7.89E-15, the plasticity is tabular every 10 MPa following the curve shown in FIGURE 9. The damage model was Ductile Damage within Abaqus, with the following parameters: Fracture strain of 0.169, Stress Triaxiality of 0, and Strain rate of 0, with linear softening, displacement based maximum degradation of 0.006774 at failure. The fracture strain and maximum degradation of

the damage models were chosen in order to cause the material to never reach over its peak stress defined at 600 MPa and 1305 MPa for the cell and cell boundaries respectively. The elements that form this body are made of Hybrid formulation, Reduced Integration, Linear, 3D Stress elements, or C3D8RH elements in Abaqus. These used a viscosity of 0.005 with an average strain kinematic split, default hourglass control, and element deletion with a max degradation of 0.9. Any wedge and tet elements that were created during the swept hex meshing technique also had the same viscosity and element deletion properties.

3 Results and Discussions

3.1 Deformation Mechanisms at the Microstructural Level

The focus of our experimentation on the 3D printed analogous materials is determining the strain field and revealing possible strain concentrations or delocalization across the different geometries. The strain field for different cell geometries, as well as the strain field of a multi-meltpool larger scale model, are measured using the DIC tests. In the following sections, deformation mechanisms in each building block, as well as the full model, will be discussed. All of these structures share a common feature of having a matrix-like cell material and a fiber-like cell boundary material. Similar to fiberglass or rebar in concrete, for a given strain, the stiffer material will take a higher stress. This is due to the fact that it has a higher Young's modulus and therefore takes more load for the same displacement. With that in mind, it makes sense that for all these structures, the higher stress is firstly found in the cell boundaries rather than the cells themselves. After the first cell boundary ruptures, the stress it was taking spreads to the surrounding cell, which is a softer material. For this reason, there is always a failure of the surrounding 2 or 3 cells depending on the geometry immediately after a cell boundary ruptures.

While stress concentrates in the stiff cell boundaries, strain concentrates in the softer cell material this is a result of the higher modulus of elasticity in the cell boundary, for a given displacement this will resist it more. For this reason, the softer material stretches more and has a higher strain, but lower stress. The microstructural features are not isotropic, two different directions of loading are considered in each case, except the inner granular structure which can be considered isotropic with acceptable accuracy.

3.1.1 Inner Granular

The inner granular block is the bulk material which covers the volume inside the meltpools in the SLM alloys (the 316L alloy as studied in this work). These sections consist of elongated hexagons of differing aspect ratios oriented in roughly the same direction. The strain distribution in this region, when subjected to a tensile load, is shown in Figure 5. As shown in this figure, the strain is delocalized by the cell boundaries. A similar distribution is also observed in the other three sections, as will be discussed in the following. The presence of the stiff material at the cell boundaries lowers the strain locally, and this mechanism will also affect the crack propagation at the microstructure as will be discussed in the following. By looking at a cluster of inner granular cells, as shown in Figure 5, a path of maximum strain is observed on an inclined direction with respect to the loading direction (load is applied on a horizontal line in this case). This line of maximum strain in all the studied cases has an angle between 30 to 60 degrees with respect to the loading direction. While this path can be attributed to the maximum shear stress, a closer look at the geometry also reveals that the strain concentration is happening along a path on which some of the cells have a semi-columnar shape. This distribution suggests that having a more concentration of equiaxial cells can significantly reduce the strain and stress concentration, and will promote a delocalization in the stress distribution.

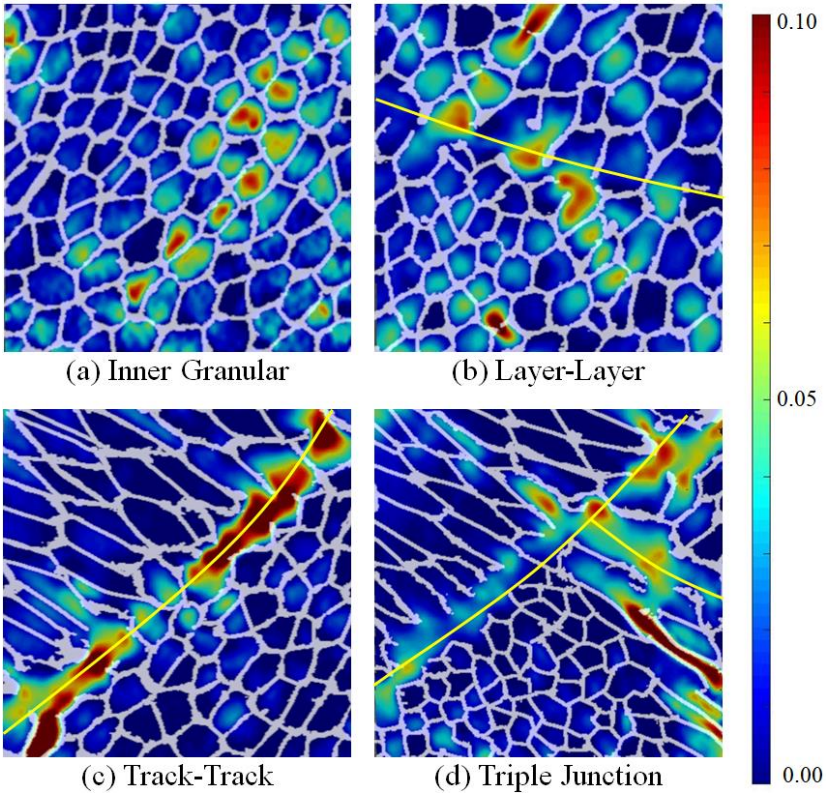

Figure 5: The strain distribution in the four base microstructures. The loading direction is horizontal for all the cases. This direction represents a loading parallel to the Layer-Layer boundaries. Meltpool boundaries are shown with yellow lines in the (b)-(d).

3.1.2 Layer-Layer Boundaries

Layer-layer meltpool boundaries are the sections of AM metals that occur in the building direction, between two layers. Two meltpools are vertically stacked atop one another, connected by these boundaries. During manufacturing, melting the material in the top layer re-melts a part of the previously solidified meltpool in the bottom layer, and this mechanism creates a complicated microstructure. In the vicinity of the layer-layer meltpool boundaries, some columnar cells are formed, and some of these cells span across the layer-layer meltpool boundary. Mechanisms behind the formation of these microstructural features are beyond the

scope of this paper. Instead, we focus on the deformation mechanisms at a microstructure directly duplicated from an SLM 316L sample. The strain distributions for the case of loading the material parallel and perpendicular to these boundaries are shown in Figures 5(b) and 6(a), respectively.

Due to the high anisotropy of this boundary, the response of the material for the aligned direction in Figure 5 and the orthogonal direction shown in Figure 6 are clearly different. In the aligned direction the strain, and consequently the stress, are relatively even across the body around the layer-layer boundary. In the case of loading the microstructure perpendicular to the layer-layer boundary, a large strain concentration is clearly observed at the vicinity of the boundary (see Figure 6a). This is a major reason behind the weakness of AM alloys when they are loaded along the building direction.

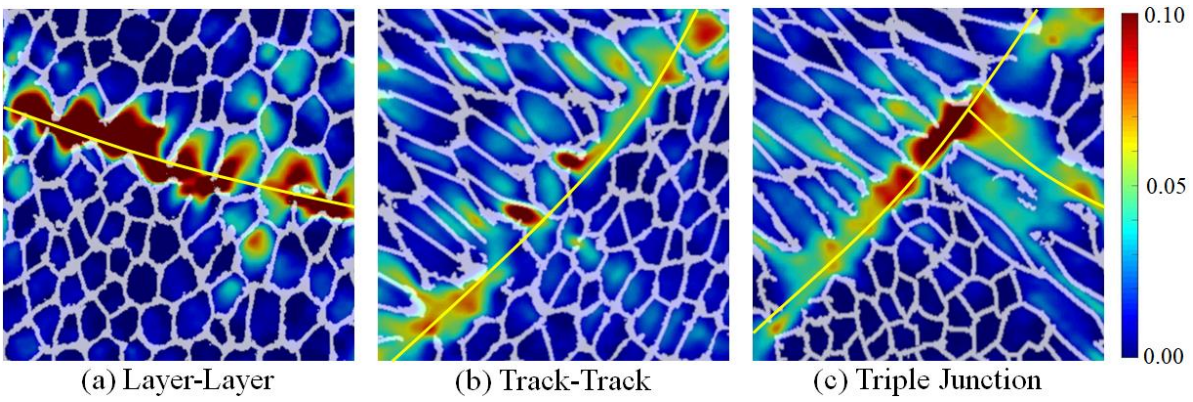

Figure 6: The strain distribution for the anisotropic structures (Layer-Layer, Track-Track, and Triple Junction). The loading direction is vertical which represents a loading perpendicular to the Layer-Layer boundaries. Meltpool boundaries with yellow lines.

3.1.3 Track-Track Boundaries

Track-track boundaries are meltpool boundaries that are formed in the build plane, where one laser track meets another laterally. These are often on a high angle due to the meltpool shape which is roughly a quarter arc of a circle. While they have a similarly stochastic nature of formation, slightly different geometry forms at the edge of the latter formed meltpool. The centers of the respective circles that form each meltpool are offset by the track width of the laser, and thus the cell boundaries form on different angles. This could be the reason for the elongated cells at the edge of the meltpools.

Regardless of the unique geometry or the formation method of track-track boundaries, larger cells are also formed at the vicinity of track-track boundaries, as can be seen in Figures 2(b) and 6(c). In the track-track meltpool boundaries, the strain is more concentrated in the larger cells with longer distance between the cell boundaries, the load path still tends to be between 30 and 60 degrees, and the strain is still interrupted by the cell boundaries as in the prior structures. As described previously, these boundaries form in the build plane laterally, and therefore the meltpool boundary is formed at 45 degrees from the build plane. This means that these structures are nearly the same in the delamination direction or the aligned direction. For this reason, these boundaries can be considered nearly the same in the aligned and the orthogonal direction.

3.1.4 Triple Junction (Vertex)

Triple junctions are positions at the microstructure where firstly a track-track boundary forms; once this boundary is formed another layer is formed atop it, and a layer-layer boundary forms above this track-track boundary. This junction can be roughly approximated as a triangle of meltpool sections, where all three have cells aligned in unique directions. This puts a central point of meltpool, which has three legs connected, the upper two of which are layer-layer boundaries, and the lower roughly perpendicular leg is a track-track boundary.

These junctions have similar weaknesses to both the layer-layer and track-track boundaries, as they are essentially formed with components of both boundaries. A large part of these junctions has no cell boundaries passing through the meltpools, therefore this structure is relatively weak. In addition, much like the track-track boundary there is always a load path through the meltpool boundaries between 30 and 60 degrees whether the load is aligned as shown in Figure 5(d) or orthogonal as shown in Figure 6(c). For this reason, this structure is relatively isotropic, especially in comparison to the layer-layer boundaries, even though it has a layer-layer boundary in its structure.

3.2 Damage Tolerance at the Microstructural Level

The combination of soft and stiff materials at the cells and cell boundaries, and also the hierarchical arrangement of the meltpools and meltpools boundaries are similar to the microstructure which is observed in some biological materials, particularly in bone and nacre. Such a microstructural arrangement is the origin of an exceptional damage tolerance in these materials, mainly because the stress concentration is delocalized at these microstructures and crack propagation is delayed by the interaction between the crack and stiff/soft boundaries. We have recently designed some defect tolerant materials by mimicking such a microstructure [42]. In this paper, we study whether such a microstructure in the SLM alloys might be utilized as a leverage for designing defect tolerant metals or not. For this purpose, a pre-crack is created at different sections of the microstructure, and by applying a small load the strain concentration and possible strain delocalization at the microstructural level are studied. This study is further expanded in Section 3.4 by loading the samples up to the point that a complete failure happens. In that case, the strength and toughness of cracked and uncracked samples are calculated and

compared, and it is shown that the hierarchical microstructure is making the material remarkably more defect tolerant compared to a single-phase material.

In order to study the strain concentration in the four micro-scale features, a pre-crack as shown in Figure 7 is created on all the samples. For comparison, the same sample is also manufactured with a single-phase material and no microstructure. All the samples are subjected to a horizontal load, and the strain distribution is calculated using the DIC method. While, the stress concentration at the crack tip for the solid geometry is clearly seen, comparing the strain distribution for the cracked microstructural features in Figure 7 with the same structures without a pre-crack (see Figure 5) shows that adding the crack is not significantly disturbing the strain distribution. The results shown in Figure 7 clearly approve that the arrangement of stiff and soft material is delocalizing the strain concentration, even in the case of having a crack in the material.

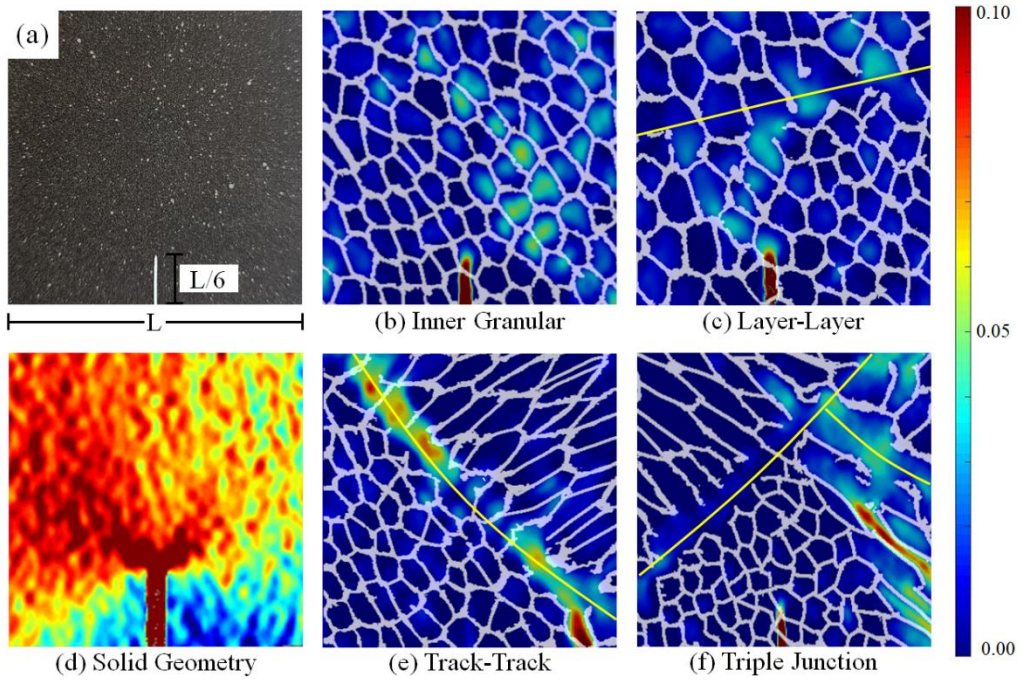

Figure 7: (a) A pre-crack is created on the samples. The strain concentration around the crack tip in a single-phase material (with no microstructure is shown in (d). The strain distribution in the cracked geometries of the 4 microstructures is shown in b, c, e, and f. Compared to the single-phase material, it is clearly observed that the microstructure delocalizes the strain concentration in the material.

In all the previous case studies, the strain distribution was reported on the sections representing the four possible microstructural features. We also have performed the same experiments on samples in which the microstructure of a larger area is considered. This sample, shown in Figure 8, has all the four structures that are studied previously within it. It encompasses five meltpools, three layer-layer boundaries, and a single track-track boundary as well as two triple junctions. In addition, both the low and high aspect ratio cells are also seen in different meltpools.

The strain distribution is this sample for four different strains is shown in Figure 8. At the early stages of loading, a slight strain concentration around the crack tip is observed. Comparing this distribution with the one observed in a single-phase material (see the strain concentration

butterfly shape in Figure 7d) clearly shows that the microstructure is delocalizing the strain concentration. However, as the loading continues, the meltpool boundaries, both the layer-layer and track-track boundaries, start deforming and a significant strain concentration is seen in those regions. While such a strain concentration can be a source of weakening the material, at the same time, the zig-zag shape of the regions with a large strain will promote a zig-zag path for the crack propagation. Propagation of the crack on an elongated path will help the structure to maintain its toughness even at the presence of cracks at the microstructural level. This mechanism is studied in more detail in the following two sections.

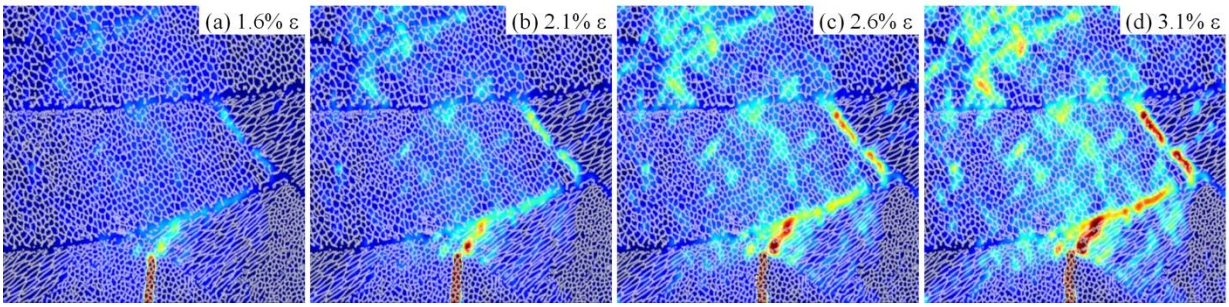

Figure 8: The strain field distribution at the microstructure at different stages of loading. While the strain concentration at the crack tip is delocalized at the early stages of loading, a strain concentration is observed at the meltpool boundaries at larger strains.

3.3 Finite element modeling to track the stress delocalization at the microstructure of AM 316L stainless steel

In Sections 3.1 and 3.2, the deformation mechanisms were studied at the microstructure of the AM alloys. In those sections, the geometry was an exact duplicate of the microstructure of AM alloys; however, to facilitate studying the deformation mechanisms we scaled up the size, and also selected two materials with a large difference between their strength and ductility (see Section 2.2). Despite the considered approximations in the size and material properties, the presented experimental results unraveled some significant unexplored fundamental deformation

mechanisms at the microstructural level in AM alloys. In this section, we will consider more realistic materials and will utilize finite element modeling to study the deformation mechanisms and the stress delocalization at the microstructure of AM stainless steel samples. The results will be compared against the experiments on the scaled models, when available. Details of modeling the microstructure, selecting the material for representing the cell and cell boundaries, and developing the finite element model are given in Section 2.4.

Similar to the previous studies, a microstructure with five meltpools, and also four levels of the zoomed-in microstructure are considered (see Figure 2 for the geometries). A pre-crack is created in the microstructure, the model is subjected to a uniaxial load, and the stress distribution at these geometries is calculated as shown in Figure 9. Interestingly, in all the sections at the microstructure, the stress concentration around the crack tip is significantly delocalized.

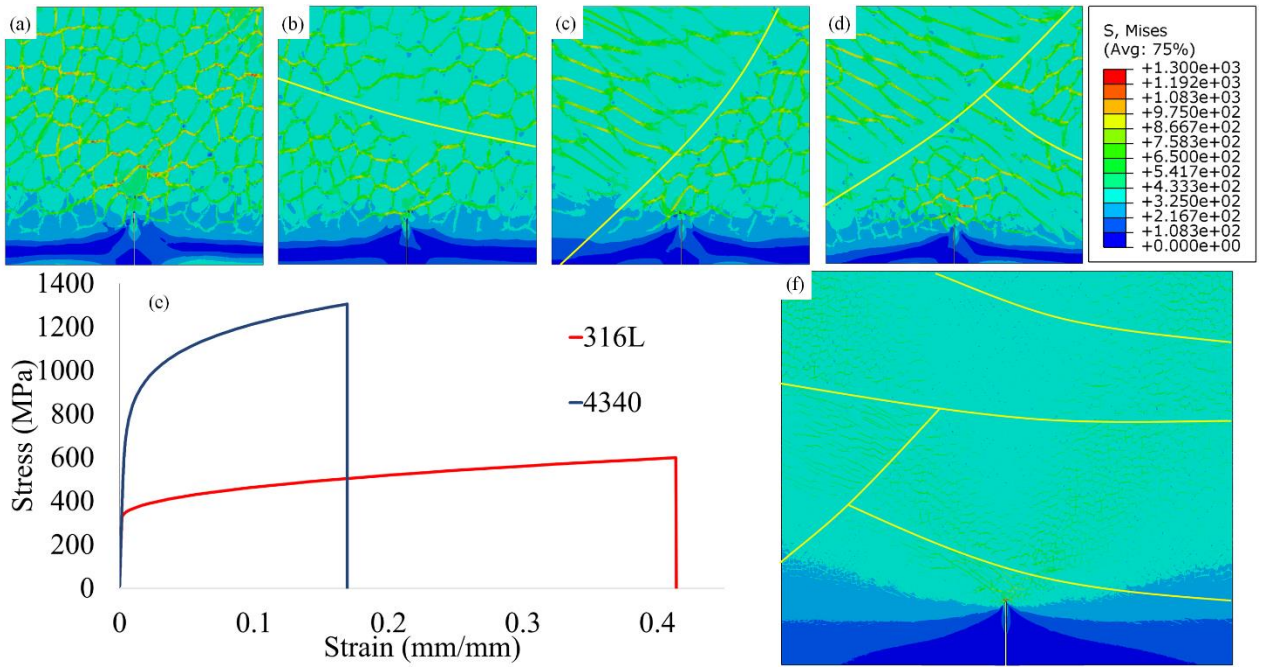

Figure 9: The stress distribution in the (a) inner granular, (b) layer-layer, (c) track-track and (d) triple junction sections of the microstructure. (e) A realistic material is considered for the material inside the cells, and at the cell boundaries (see Section 2.5). The stress distribution is also shown in a full model consisting of five meltpools (f). In all the section, a stress delocalization is clearly observed, since there is no stress concentration at the crack tip.

In comparison to the experimental samples, the FEA models have a higher stress concentration at the tip of the crack. This stems from the more realistic materials used in the FEA model than the experimental models. The stress-strain responses for the material at the cell and cell boundaries are shown in Figure 9e (see the discussion about the selection of materials in Section 2.4). In the experiments, the extreme difference of the softness of the TangoBlackPlus compared to the VeroWhitePlus causes nearly all of the stress to be taken by the cell boundaries in a lattice-like pattern. As the 316 and 4340 used in the FEA are far closer in stiffness and material properties,

this leads to the stress more evenly spread across the entire body rather than just the cell boundaries alone.

3.4 Crack propagation and damage tolerance

The observed stress delocalization at the microstructure can trigger a damage tolerance in the material. In addition, the stacking of the material in a hierarchical structure in the arrangement of cells, cell boundaries, meltpools, and meltpool boundaries, will elongate the path for the crack to propagate in the microstructure. These mechanisms strongly improve the material's capability to retain its strength and ductility even when some cracks are present. To investigate the damage tolerance and crack propagation at the microstructure, the cracked samples (the full sample in the experiment and also the samples in the finite element model) are further loaded until the final fracture of the material happens. In each case, the crack propagation path is tracked, and also the stress-strain response is measured. The response of samples with the microstructure of an AM alloy is compared against a sample with a single-phase to investigate the effect of microstructure on the mechanical properties of the material.

Crack propagation in the four sections of the microstructure is shown in Figure 10(a-d). It is clearly shown that the crack path follows the microstructural features, and for this reason, compared to a single-phase material, the crack path is longer in the geometries with this hierarchical microstructure. For the inner granular structure (Figure 10a), the crack mostly follows the cell boundaries, although, in some regions, transgranular propagation also happens. Also, similar to the strain concentration (see Figure 5a), the crack propagation also follows the direction in which the cells are slightly elongated.

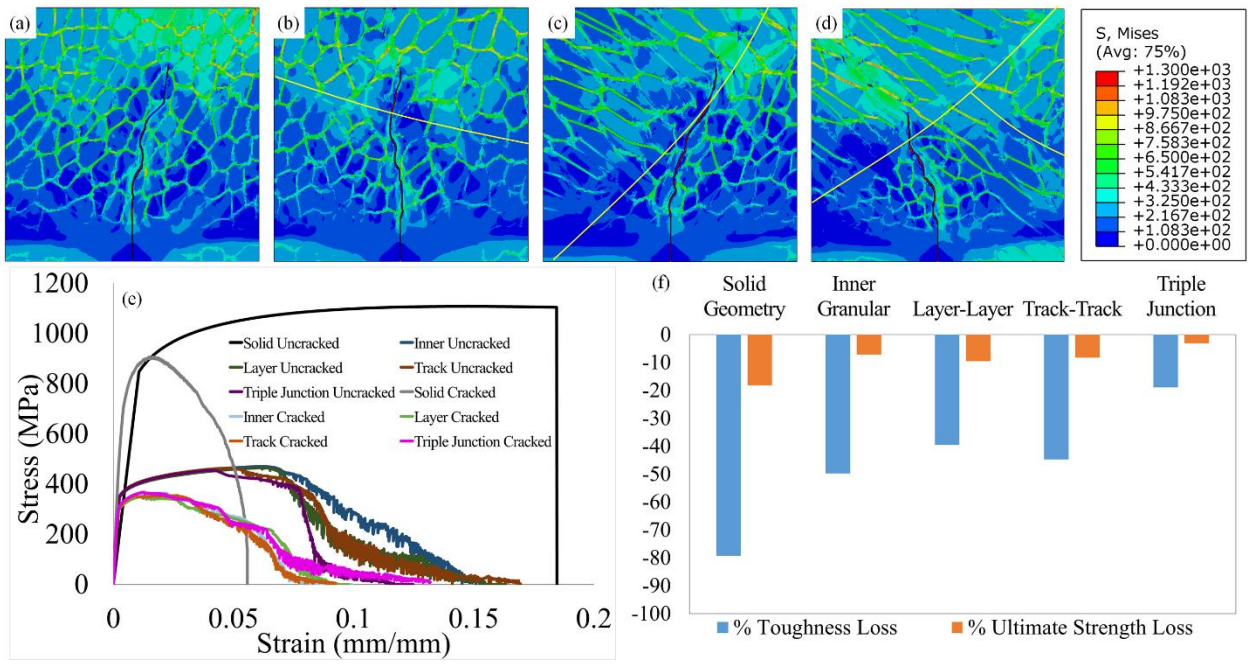

Figure 10: (a-d) The crack propagation path in the four sections of microstructure. The stress-strain response for each microstructure is measured for the same samples with and without pre-cracks. The same response is also measured for a single-phase material. The loss of strength and toughness before and after adding a pre-crack is compared for a single-phase material and the four sections of the microstructure in (f). A single-phase (Solid Geometry) material loses 18% of its strength and 79% of the toughness by creating a pre-crack, the inner granular, layer-layer, track-track, and triple junction microstructures lose approximately 7%, 9%, 8%, and 3% of the original strength and 50%, 40%, 45%, and 19% of the toughness in the presence of a pre-crack with the same length.

In the layer-layer microstructure, shown in Figure 10(b), the structure fails in a line passing through the meltpool boundary. The crack path takes advantage of similar failure methods as the inner granular structure (following the cell boundaries), failing through the long straight cells, and in this case the meltpool boundary itself. The loading fails mostly the horizontal cell

boundaries which are the logical path of least resistance for the crack. It takes far fewer timesteps for it to fail within the second half of the material once it reached the meltpool boundary, as a result of the longer cells and fewer boundaries past the layer-layer boundary. At the final few cell boundary failures, the crack circumvents the cell boundary that is directly in its path. This is a physical example of the cell boundaries reducing the ability of the crack to fail the part. The more paths it has of this nature that force it to go sideways the higher the fracture resistance of the material as a whole becomes.

For the track-track sample, there is a similar beginning as the others as shown in Figure 10(c). There are two unique features that were not present in the prior substructures: an angled meltpool boundary and the elongated cells. The angled meltpool boundary offers both improving and weakening effects on the way of crack propagation. For the improving aspect, the boundary forces the crack to act on the angle of the meltpool boundary, in which only the cosine portion of the force cracking the body is actually expanding the crack. Negatively, this is a much longer section of the body whereby there is a large swath of cell material with no boundary blocking crack growth. This leads to a much easier spread of cracks down the meltpool boundary itself. These two factors compete, the longer cells leading to a weaker material, and the misaligned path leading to a stronger material. The other unique facet of this substructure is the elongated cells on the left side of the image. These cells are more aligned with the loading direction, and thus this half of the body is stiffer than the right half. For that reason, more flexion is present in the right half which also contributes to the misaligned crack.

Triple junctions (Figure 10d) have the most unique features as mentioned in the experimentation section above. The highly elongated cells, longer distances between cell boundaries, and the three meltpool boundaries at different angles lead to a multitude of differences between this and

the other substructures. In this case, the initial failure and crack concentration is similar to the other sections in the microstructure. Different features of the crack propagation show up when the material starts to fail and the crack propagates toward the triple junction. At the vicinity of a triple junction, there is a much more prevalent redirection of the crack to a higher angle as shown in Figure 10(d). The material fails through the inner granular section on the bottom near the crack until it reaches one of the meltpool boundaries. From this point, the crack is diverted at a 45-degree angle from the vertical direction, meaning only 70% of the load applied horizontally is taken into stretching the crack wider. This certainly helps to have a higher toughness response, but similar to the track-track meltpool boundary, there are much longer cells with increasing distance between the cell boundaries which would have a negative impact on toughness.

Solid geometry bodies lose a significant amount of their strength and toughness when a pre-crack is added in their structure. However, the above-mentioned mechanisms which delay the crack propagation by lengthening the crack path will help the material to retain its toughness in the presence of cracks at the microstructural level. At the same time, the stress delocalization, as studied in Section 3.3 will help the material to retain its strength, even when there are microcracks in the material. These effects are studied by tracking the stress-strain response of the material, as shown in Figure 10(e) and (f). As shown in Figure 10(e), for each section of the microstructure, the stress-strain response is plotted for the structures with and without a pre-crack. The same study is also performed for a single-phase material without the hierarchical microstructure.

The results are summarized in Figure 10(f) which shows the drop in the strength and toughness by having a pre-crack in each of the materials. Based on the assertions, this multi-material microstructure all have a far lower strength and toughness loss from an uncracked body to a

cracked body. As shown, while a sample made of the single-phase loses approximately 18% of its strength by having a notch (the cracked sample maintains 82% of the original strength), the inner granular, layer-layer, track-track, and triple junction microstructures maintain approximately 93%, 90%, 92% and 97% of the original strength in presence of a pre-crack with the same length. A similar improvement is also observed in maintaining the toughness at all the sections of microstructures, as shown in Figure 10(g). The results show that the cracked sample with a microstructure loses 3.7% of its toughness and 29% of its strength vs the uncracked structure, which is a substantial improvement compared to the single-phase material which loses 61% of its toughness and 52% of its strength. As discussed earlier, these responses are both connected to the stress delocalization and the hierarchical arrangement of stiff-soft phases in the microstructure.

To further investigate these mechanisms, a new representative sample is 3D printed, with scaling up the microstructure. In this sample, the difference between the stiffness of the material which represents the cell and cell boundaries is less, compared to the results of Sections 3.1 and 3.2. This change in the material properties helps us better track the crack path, while it will not change the fundamental deformation mechanisms which are prominently a function of the microstructure. Samples with and without pre-cracked are pulled and the stress-strain responses are recorded for both the samples (see **Error! Reference source not found.**).

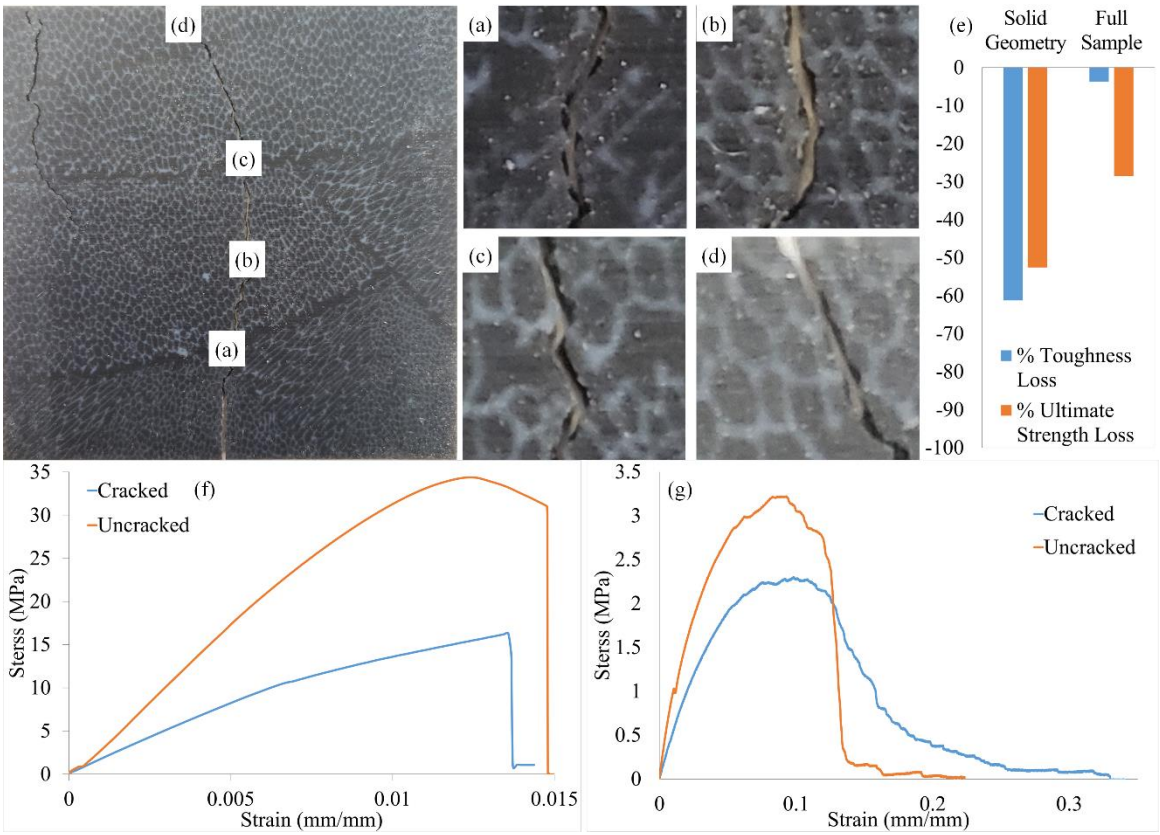

Figure 11: (a-d) The crack propagation at different sections in the microstructure of 3D printed alloys. The arrangement of stiff and soft phases elongates the crack propagation as shown by the jagged uneven crack path. This mechanism helps the material to maintain its strength and toughness. (e) While the single-phase material loses 52% of its strength, the material with the microstructure only loses 29% of its strength. Also, when the single-phase material can maintain only 39% of its initial toughness, the microstructure helps the material to maintain 96.3% of its toughness when a pre-crack is created in the structure. The stress-strain response of the material with a single-phase and the material with a microstructure are shown in (f) and (g).

The crack propagation path in the sample with a pre-crack is shown in **Error! Reference source not found.**. As shown in sets a-d, similar crack propagation mechanisms compared to the finite

element simulations are observed. The path is a combination of sections in which the crack follows the cell boundaries, and also regions where the crack passes through a cell. However, the crack mostly follows the cell boundaries, which elongates the length of the crack propagation path. By comparing the stress-strain response of single-phase samples, with samples that had the microstructure (see the curves in **Error! Reference source not found.**(f) and (g)), it is observed that while the strength and toughness drops by 52% and 61% in a single-phase material, the microstructure remarkably improves the defect tolerance in the material such that the toughness only drops by 4% in the material with the hierarchical structure. The microstructure helps the material to maintain 96% of its toughness even when a large crack (the crack length is $1/6^{th}$ of the sample width) in the material. The microstructure also makes the material maintain 71% of its strength which is a significant improvement compared to the single-phase material.

4 Conclusion

In this paper, the deformation mechanisms at the microstructure of AM alloys are studied using both experimental and computational methods. The strain distributions in four sections of the microstructure (inner granular, track-track boundaries, layer-layer boundaries, and triple junction points inside the meltpools) are studied. In addition, the stress concentration at the vicinity of a micro-crack in each of these sections was studied as were crack propagation mechanisms at the microstructural level. Our results show that the cellular structure and the hierarchical arrangement of stiff and soft phases at the microstructure of AM alloys delocalize the stress concentration at the vicinity of possible defects in the material. In the case of having cracks in the microstructure, the arrangement of different phases at the microstructure elongates the crack propagation path. Stress delocalization and elongation of the crack propagation path significantly

improves the defect tolerance at the microstructural level. A material with this specific microstructure can retain a large portion of its original strength and toughness in the presence of large cracks at the microstructure. Using the already discovered relationships between the processing parameters and the microstructure in AM printing of alloys, our results can be utilized as a tool in engineering the microstructure to fabricate metals with improved mechanical properties, particularly exceptional defect tolerance.

References

1. Yadroitsev, I., et al., *Energy input effect on morphology and microstructure of selective laser melting single track from metallic powder.* Journal of Materials Processing Technology, 2013. **213**(4): p. 606-613.

2. Wei, Y.J., et al., *Evading the strength- ductility trade-off dilemma in steel through gradient hierarchical nanotwins.* Nature Communications, 2014. **5**: p. 8.

3. Tucho, W.M., et al., *Investigation of effects of process parameters on microstructure and hardness of SLM manufactured SS316L.* Journal of Alloys and Compounds, 2018. **740**: p. 910-925.

4. Sun, Z.J., et al., *Simultaneously enhanced strength and ductility for 3D-printed stainless steel 316L by selective laser melting.* Npg Asia Materials, 2018. **10**: p. 10.

5. Song, B., et al., *Differences in microstructure and properties between selective laser melting and traditional manufacturing for fabrication of metal parts: A review.* Frontiers of Mechanical Engineering, 2015. **10**(2): p. 111-125.

6. Shrestha, S., S. Rauniyar, and K. Chou, *Thermo-Fluid Modeling of Selective Laser Melting: Single-Track Formation Incorporating Metallic Powder.* Journal of Materials Engineering and Performance, 2019. **28**(2): p. 611-619.

7. Saeidi, K., et al., *Austenitic stainless steel strengthened by the in situ formation of oxide nanoinclusions.* Rsc Advances, 2015. **5**(27): p. 20747-20750.

8. Saeidi, K. and F. Akhtar, *Subgrain-controlled grain growth in the laser-melted 316 L promoting strength at high temperatures.* Royal Society Open Science, 2018. **5**(5): p. 7.

9. Liverani, E., et al., *Effect of selective laser melting (SLM) process parameters on microstructure and mechanical properties of 316L austenitic stainless steel.* Journal of Materials Processing Technology, 2017. **249**: p. 255-263.

10. Jung, H.Y., et al., *Fabrication of Fe-based bulk metallic glass by selective laser melting: A parameter study.* Materials & Design, 2015. **86**: p. 703-708.

11. Taylor, S.L., et al., *Iron and Nickel Cellular Structures by Sintering of 3D-Printed Oxide or Metallic Particle Inks.* Advanced Engineering Materials, 2017. **19**(11): p. 8.

12. Libonati, F., et al., *Bone-Inspired Materials by Design: Toughness Amplification Observed Using 3D Printing and Testing.* Advanced Engineering Materials, 2016. **18**(8): p. 1354-1363.

13. Dadbakhsh, S., et al., *Effect of SLM Parameters on Transformation Temperatures of Shape Memory Nickel Titanium Parts.* Advanced Engineering Materials, 2014. **16**(9): p. 1140-1146.

14. Lewandowski, J.J. and M. Seifi, *Metal Additive Manufacturing: A Review of Mechanical Properties*, in *Annual Review of Materials Research, Vol 46*, D.R. Clarke, Editor. 2016, Annual Reviews: Palo Alto. p. 151-186.

15. Alshare, A.A., F. Calzone, and M. Muzzupappa, *Hydraulic manifold design via additive manufacturing optimized with CFD and fluid-structure interaction simulations.* Rapid Prototyping Journal, 2019. **25**(9): p. 1516-1524.

16. Soro, N., et al., *Evaluation of the mechanical compatibility of additively manufactured porous Ti-25Ta alloy for load-bearing implant applications.* Journal of the Mechanical Behavior of Biomedical Materials, 2019. **97**: p. 149-158.

17. Sotov, A.V., et al., *Investigation of the Ni-Co-Cr alloy microstructure for the manufacturing of combustion chamber GTE by selective laser melting.* International Journal of Advanced Manufacturing Technology, 2019. **101**(9-12): p. 3047-3053.

18. Ahmadi, A., et al., *Effect of manufacturing parameters on mechanical properties of 316L stainless steel parts fabricated by selective laser melting: A computational framework.* Materials & Design, 2016. **112**: p. 328-338.

19. Choi, J.P., et al., *Densification Behavior of 316L Stainless Steel Parts Fabricated by Selective Laser Melting by Variation in Laser Energy Density.* Materials Transactions, 2016. **57**(11): p. 1952-1959.

20. Farshidianfar, M.H., A. Khajepour, and A.P. Gerlich, *Effect of real-time cooling rate on microstructure in Laser Additive Manufacturing.* Journal of Materials Processing Technology, 2016. **231**: p. 468-478.

21. Kunze, K., et al., *Texture, anisotropy in microstructure and mechanical properties of IN738LC alloy processed by selective laser melting (SLM).* Materials Science and Engineering a-Structural Materials Properties Microstructure and Processing, 2015. **620**: p. 213-222.

22. Wang, Y.M., et al., *Additively manufactured hierarchical stainless steels with high strength and ductility.* Nature Materials, 2018. **17**(1): p. 63-+.

23. Rannar, L.E., et al., *Hierarchical structures of stainless steel 316L manufactured by Electron Beam Melting.* Additive Manufacturing, 2017. **17**: p. 106-112.

24. Zhong, Y., et al., *Intragranular cellular segregation network structure strengthening 316L stainless steel prepared by selective laser melting.* Journal of Nuclear Materials, 2016. **470**: p. 170-178.

25. Yasa, E. and J.P. Kruth, *Microstructural investigation of Selective Laser Melting 316L stainless steel parts exposed to laser re-melting*, in *1st Cirp Conference on Surface*

Integrity, E. Brinksmeier, I.S. Jawahir, and D. Meyer, Editors. 2011, Elsevier Science Bv: Amsterdam.

26. Saeidi, K., et al., *Transformation of austenite to duplex austenite-ferrite assembly in annealed stainless steel 316L consolidated by laser melting.* Journal of Alloys and Compounds, 2015. **633**: p. 463-469.

27. Prashanth, K.G. and J. Eckert, *Formation of metastable cellular microstructures in selective laser melted alloys.* Journal of Alloys and Compounds, 2017. **707**: p. 27-34.

28. Saeidi, K., et al., *Hardened austenite steel with columnar sub-grain structure formed by laser melting.* Materials Science and Engineering a-Structural Materials Properties Microstructure and Processing, 2015. **625**: p. 221-229.

29. Nguejio, J., et al., *Comparison of microstructure features and mechanical properties for additive manufactured and wrought nickel alloys 625.* Materials Science and Engineering a-Structural Materials Properties Microstructure and Processing, 2019. **764**: p. 12.

30. Li, X.W., et al., *Heterogeneously tempered martensitic high strength steel by selective laser melting and its micro-lattice: Processing, microstructure, superior performance and mechanisms.* Materials & Design, 2019. **178**: p. 13.

31. Aboulkhair, N.T., et al., *3D printing of Aluminium alloys: Additive Manufacturing of Aluminium alloys using selective laser melting.* Progress in Materials Science, 2019. **106**: p. 45.

32. Chen, J.Y., Y. Huang, and M. Ortiz, *Fracture analysis of cellular materials: A strain gradient model.* Journal of the Mechanics and Physics of Solids, 1998. **46**(5): p. 789-828.

33. Liu, X.H., et al., *Morphological Development of Sub-Grain Cellular/Bands Microstructures in Selective Laser Melting.* Materials, 2019. **12**(8): p. 16.

34. Dong, Z.C., et al., *Study of Size Effect on Microstructure and Mechanical Properties of AlSi10Mg Samples Made by Selective Laser Melting.* Materials, 2018. **11**(12): p. 14.

35. Peters, W.H. and W.F. Ranson, *DIGITAL IMAGING TECHNIQUES IN EXPERIMENTAL STRESS-ANALYSIS.* Optical Engineering, 1982. **21**(3): p. 427-431.

36. Li, X.M., et al., *H-DenseUNet: Hybrid Densely Connected UNet for Liver and Tumor Segmentation From CT Volumes.* Ieee Transactions on Medical Imaging, 2018. **37**(12): p. 2663-2674.

37. Al Arif, S., K. Knapp, and G. Slabaugh, *Fully automatic cervical vertebrae segmentation framework for X-ray images.* Computer Methods and Programs in Biomedicine, 2018. **157**: p. 95-111.

38. Chan, J.W., et al., *A convolutional neural network algorithm for automatic segmentation of head and neck organs at risk using deep lifelong learning.* Medical Physics, 2019. **46**(5): p. 2204-2213.

39. Bass, L., N.A. Meisel, and C.B. Williams, *Exploring variability of orientation and aging effects in material properties of multi-material jetting parts.* Rapid Prototyping Journal, 2016. **22**(5): p. 826-834.

40. Blaber, J., B. Adair, and A. Antoniou, *Ncorr: Open-Source 2D Digital Image Correlation Matlab Software*. Experimental Mechanics, 2015. **55**(6): p. 1105-1122.

41. Jiang, W.G., et al., *Homogenized Finite Element Analysis on Effective Elastoplastic Mechanical Behaviors of Composite with Imperfect Interfaces.* International Journal of Molecular Sciences, 2014. **15**(12): p. 23389-23407.

42. Mirzaeifar, R., et al., *Defect-Tolerant Bioinspired Hierarchical Composites: Simulation and Experiment.* Acs Biomaterials Science & Engineering, 2015. **1**(5): p. 295-304.

The Optimal Geometry of Sub-grain Microstructural Features in 3D Printed Alloys for Improving the Strength and Toughness

Matthew Moneghan

ABSTRACT

Mechanical properties of 3D printed alloys are highly related to their microstructural properties. While in the past few years a large effort has been dedicated to finding the relationship between the processing parameters and mechanical properties, a systematic methodology that considers the effect of microstructure on the mechanical properties is still missing. In this paper, a parametric study is performed to investigate how the geometry of cells, sub-grain microstructures that form during 3D printing of alloys, affects the strength and toughness of the material. Our results can be used to find out the optimum geometry of the cells for any specific loading condition, and the targeted material properties (strength or toughness). The previously reported works which define the interconnection between the processing parameters and the microstructure can then be used to find the processing parameters which can be used to 3D print the alloy with those optimum mechanical properties. Our results can also be used as a guide for the community for designing processing parameters which can be used to modify the 3D printing strategies for fabricating metals with the microstructures which correspond to the optimal mechanical properties.

GENERAL AUDIENCE ABSTRACT

Parts that are printed through the SLM technique have a cellular network of stiff material spread through the whole part. These cellular boundaries have an increased stiffness and strength with respect to the cells, thus leading to a multi-material distribution within the part; this network leads to increased damage tolerance. The sizes and shapes of the cells that form this network can be changed and optimized in order to change bulk material properties including the toughness and strength of the bulk parts. The different types of cells that make up this network are parameterized in this paper and are optimized within a design space for maximum strength and toughness. These optimal cellular shapes are presented and explained within the work. Once the best cellular shapes are known, these can be implemented into the creation of new SLM parts such that parts can be fabricated with increased material properties for the task the part needs to complete.

Table of Contents

1 Introduction

As problems grow more complex in the current day and age, new solutions are continuously being researched and developed in order to take on these challenges. One such focus that has grown within the last decade is additive manufacturing (AM). Polymer printing grew quickly and gained widespread attention for small scale prototyping and modeling; recently additively manufacturing metals through the selective laser melting (SLM) process has been a focus of the automotive, aerospace, and biomedical industries [1-13]. These industries are using these technologies to create more capable and efficient parts than subtractive manufacturing can [14]. While normal bulk-produced metals forms such as castings, extrusions, or sheets have grains as their main microstructural feature, SLM printed metals can have two more features: meltpools and cells. Meltpools are well-studied phenomena, and occur when the powered laser melts a path of metal powder which then cools to form an extruded semi-circular shape through the material [15-18]. Cells, on the other hand, are far more complex and still in the process of being studied to understand exactly how they form, what they are, and what they impact at a bulk-part level. Cells are sub-granular structures that form a multi-material and possibly multi-phase system inside meltpools [19-22]. Due to the proposed elemental makeup of the cell and cell boundaries, the cell geometry influences the macro properties of SLM printed parts [23-25]. These cells are complicated by the fact that they form across meltpools as well, forming cell shapes that can be categorized into three base structures: inner granular cells, epitaxial cells, and non-epitaxial cells. Normal inner granular cells are roughly hexagonal, with one set of parallel faces elongated as demonstrated in Figure 12 (a) and (d). The epitaxial cells are a stretched version of inner granular cells where the elongated faces are extended across a layer-layer meltpool boundary in the build direction. In grain growth, grains that grow across a meltpool, perpendicularly, are

considered epitaxial. Cells cross the boundary in the same manner, and thus get the same name; these cells can be seen in Figure 12 (b) and (e). Non-epitaxial cells are ones that grow across a boundary on some non-perpendicular angle. This often occurs on Track-Track meltpool boundaries as these boundaries are roughly 45 degrees from the build direction. These cells are more complex in shape, as it forms when a meltpool forms its outermost cells perpendicularly to the previously formed cells on the prior laser path; this leads to the shape in Figure 12 (c) and (f). With these three different structures, and the knowledge that they influence macro-properties of the material, we sought out an improvement of the current sizing that we have in order to improve our materials. It is worth noting that the size and shape of these cells can be controlled by tailoring the processing parameters during 3d printing.

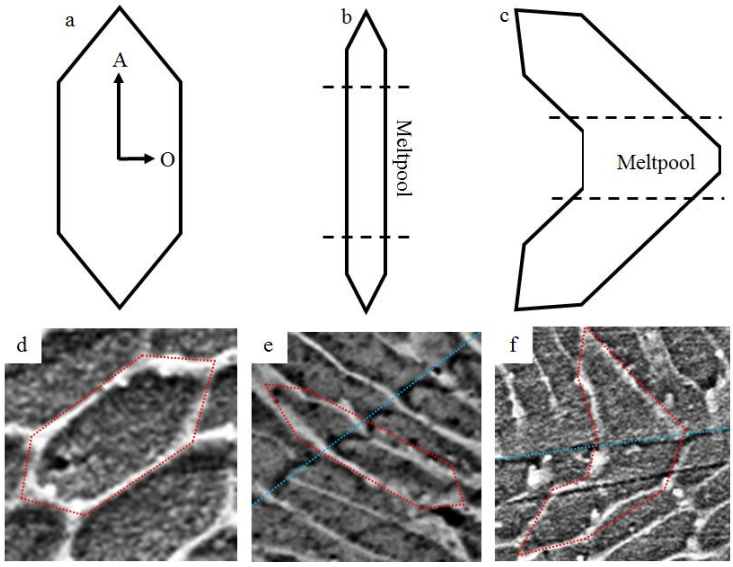

Figure 12: Ideal (a) inner granular, (b) epitaxial, and (c) non-epitaxial cells. SEM images of these three cells are shown in (d) to (f). The cell and meltpool boundaries are shown with red and blue, respectively. Loading directions for use in the simulations are defined as aligned (A) and orthogonal (O) as shown with the two arrows.

2 Methods

In order to optimize or improve a given geometry, it needs to be split into parameterized sections that can be controlled and adjusted. For this reason, each of the geometries was split into a set of modifiable parameters which are defined as the following (see Figure 13): Width (W) is the distance of the inside of the cell in the non-elongated direction; Height (H) is the overall distance from tip to tip of the cell in the elongated direction; Length (L) is the "tip length" of the cell, so distance from the tip of one side, to the beginning of the middle faces in the elongated direction; Thickness (T) is the cell boundary thickness between two parallel faces of any two cells. Lastly, the non-epitaxial cells have another feature which is the angle between the cell centerline and the horizontal direction (θ).

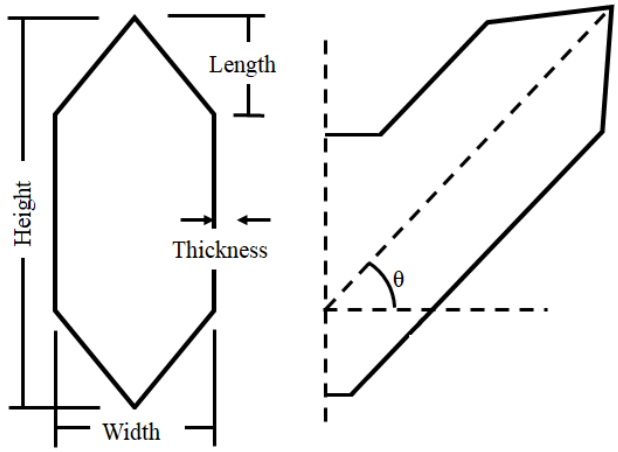

Figure 13: Ideal inner granular and non-epitaxial cells with parameters defined geometrically

2.1 Parameterization Values

For these simulations, a wide range of parameters could have been changed through a continuous value range. In order to make this analysis feasible to run and solve, three levels were assigned for each parameter. Using ImageJ and images taken from SEM of our AM metal samples, average values of height (H), width (W), length (L), thickness (T), and Theta (θ) were measured

for the respective structures. Height, width, length, and thickness were varied ± 15% of their average values, while the θ value varied around 45º ± 5º.

Sensitivity studies were performed on all three structures in both loading conditions to show which parametric variables had the highest and lowest impacts without interactions. These studies showed that on the inner granular aligned direction, the H, W, and L had the most impact; for the orthogonal direction, all of the variables had a strong influence. For the non-epitaxial aligned direction, the height, thickness, and θ values had the most impact, while the orthogonal direction showed the W, L, T, and θ had the strongest impact. In the epitaxially aligned direction the W, L, and T mattered the most. Lastly, the orthogonal direction of the epitaxial cells shows that the H, W, and L matter the most. For the sake of reducing simulation time and computation power required for this analysis, only the variables mentioned above were analyzed while the others were held constant. The summary of these values, including what was held constant versus changed for each case is shown in Table 1.

Table 1: Display of what values were parameterized versus those held constant for each of the simulations based on the sensitivity analysis performed, all the units given are in micrometers for the height, width, length, and thickness, and degrees for θ.

	Inner Granular						Epitaxial						Non-Epitaxial					
	Aligned			Orthogonal			Aligned			Orthogonal			Aligned			Orthogonal		
Height	1.241	1.460	1.679	1.241	1.460	1.679	6.253			5.746	6.253	6.760	1.241	1.460	1.679	0.124		
Width	0.434	0.510	0.587	0.434	0.510	0.587	0.714	0.777	0.840	0.714	0.777	0.840	0.434			0.434	0.510	0.587
Length	0.451	0.530	0.610	0.451	0.530	0.610	0.782	0.851	0.920	0.782	0.851	0.920	0.451			0.451	0.530	0.610
Thickness	0.089	0.105	0.121	0.089	0.105	0.121	0.089	0.097	0.105	0.097			0.089	0.105	0.121	0.089	0.105	0.121
Theta	---			---			---			---			40	45	50	40	45	50

2.2 Finite element approach

For the analysis done within this study, the failure mechanisms of these cellular structures need to be accurately represented. This dependence is based on the fact that the cell boundary and cell have two different elemental makeups, and therefore different mechanical properties [19, 23].

The topic of the exact material composition, phase, and precise characteristics of these cells and boundaries are debated within the community, but it is generally accepted there is a higher concentration of some elements in the cell boundaries, namely nickel, silicon, chromium, and molybdenum. These are generally stiffening and hardening agents in steel, and thus this boundary structure is proposed to be a stronger and more brittle material [24]. In this work, two representative materials are used for the cell and cell boundary respectively. For the cell, a Ramberg-Osgood curve of 316L steel is used. The cell boundary uses a stiffer and stronger material, similar to 4340. This custom material kept the same elasticity curve but extended a Ramberg-Osgood model of 4340 to a higher ultimate strength such that the toughness was equivalent to the 316L model. While these two materials do not perfectly represent the cell and cell boundary, they are analogous materials that can show off the deformation and failure modes of these structures and let us characterize and compare the different shapes among one another in order to determine ideal geometric characteristics.

2.3 Mesh convergence

A mesh convergence study is done on each of the six models, whereby a finer and finer mesh is used until a threshold of accuracy is passed going from one model to the next [26]. For this study, the convergence criterion is 5%. Once the difference between the studied parameter (in this case toughness) changes by less than 5% the mesh is deemed converged. The seed size at convergence and the percentage difference to the next finest mesh size for each case is shown in Table 2.

Table 2: Mesh convergence table showing the converged seed size for each respective study, and the percentage difference to the next smallest seed size; the seed sizes are given in micrometers.

Study	Seed Size	% Difference
Inner Aligned	0.040	0.80
Inner Orthogonal	0.050	0.36
Epitaxial Aligned	0.050	1.31
Epitaxial Orthogonal	0.045	0.63
Non-Epitaxial Aligned	0.020	2.57
Non-Epitaxial Orthogonal	0.020	0.63

3 Results and Discussion

Materials at bulk levels can be characterized by many values and outputs, in this study we chose to analyze for the toughness and the maximum average strength these structures have based on their respective microstructural parameters. Damage tolerance comes from having a high toughness which is already a combination of the overall elongation and the max strength of the material [27]. Maximum strength is relevant, as many materials are chosen not for their ability to absorb energy, but rather how much load they can withstand before yielding. All of these structures are parameterized to the point where they are anisotropic, and thus are tested in both directions in plane. For this work, there are two directions tested for each of these structures which are referred to as the aligned and orthogonal direction. (see Figure 1 and 3).

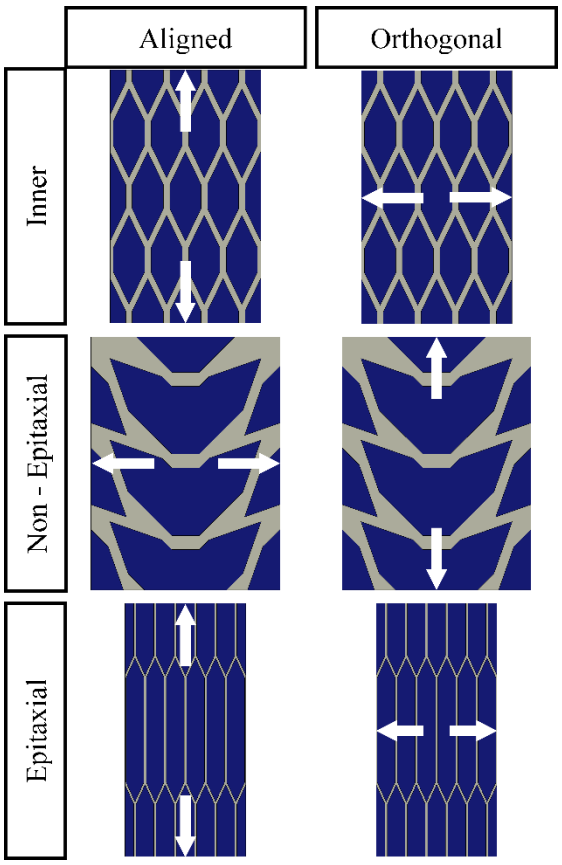

Figure 14: The median-valued geometry of each structure, shown in both the aligned and orthogonal loading conditions. The cell interior and the cell boundaries are shown with dark blue and gray, respectively.

These structures all have a high variation across the different parameterized conditions, which lead to different geometric shapes having improved properties in either toughness or strength. These results are split by the structure type (inner granular, non-epitaxial, and epitaxial), loading direction (aligned and orthogonal), and the strength and toughness. The geometries with the highest and lowest values were studied, and each case is shown together in Figure 15.

For the majority of the simulations, there are 3 influencing variables for the toughness and strength, respectively. In the following sections, contour plots are used to study the effect of geometric parameters on the mechanical parameters for which the colors correspond to the

strength or toughness. The X and Y axes are two of the geometrical features as labeled accordingly, and there is a third variable that is unlabeled. In each column of 3 contour plots, the unlabeled value changes from its minimum value to its maximum value. In this method, all data points and trends are shown, with a smooth contour that averages between the calculated values.

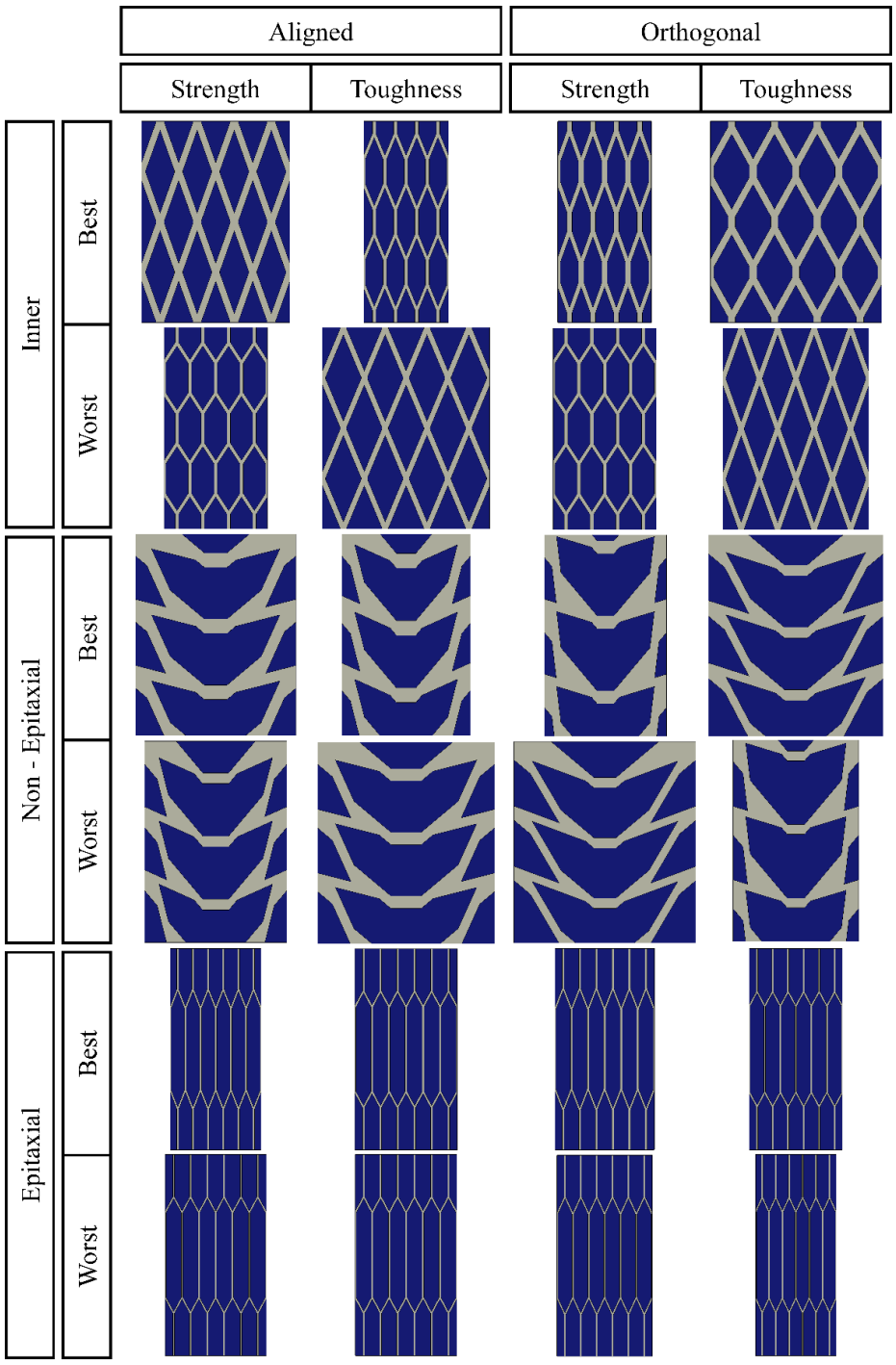

Figure 15: A comparison of each of the structures, loading directions, and criteria studied for the best and worst geometric conditions based on the parameterization defined in the following sections.

3.1 Toughness

Toughness of a given material is assessed as a function of how much energy it can absorb before failing or reaching a given limit. Having a high toughness means that structure has a good combination of strength and elongation leading to increased fracture resistance. The toughness is also directly related to the damage tolerance of the parameterized structures. In the following sections, a parametric study is performed to find the effect of changing each of the geometrical aspects of the cells on the toughness. Each of the cell types and loading directions are analyzed separately. In the following contour plots for toughness, units are in MJ/m^3.

3.1.1 Inner granular cells

The inner granular cells are the bulk of the material, which cover a significant portion of the meltpools, and the 3D printed part. In this case, inner granular structures are very regular shapes that essentially go from diamonds at a high length with low height, to nearly long rectangles with a high height and low length; for images of both see Figure 15. An initial sensitivity analysis shows that in the aligned direction, the toughness is prominently influenced by height, width, and length of the cells. The trend of changing the toughness with respect to these three major geometrical features in the cells is shown in the nine panels in Figure 16. The results are reflected in the optimum shape of the cells with the highest toughness as shown in Figure 15. Toughness is improved by having long thin cells, which leads to cell boundaries that are similar to oriented fibers of a fiber-based composite. This makes sense as this means the load can be transferred through the long thin cell boundaries between the cells. Once these thin boundaries break, softer material can continuously deform to achieve a high deformation, and the material will possess a high toughness. The worst structures (least toughness), in this case, had a high width and length with a low height, leading to more diamond-shaped structures. These structures are able to withstand a much higher maximum load, and thus break much faster when they begin

to fail. This leads to reduced elongation in comparison with the higher-toughness structures, and thus lower toughness.

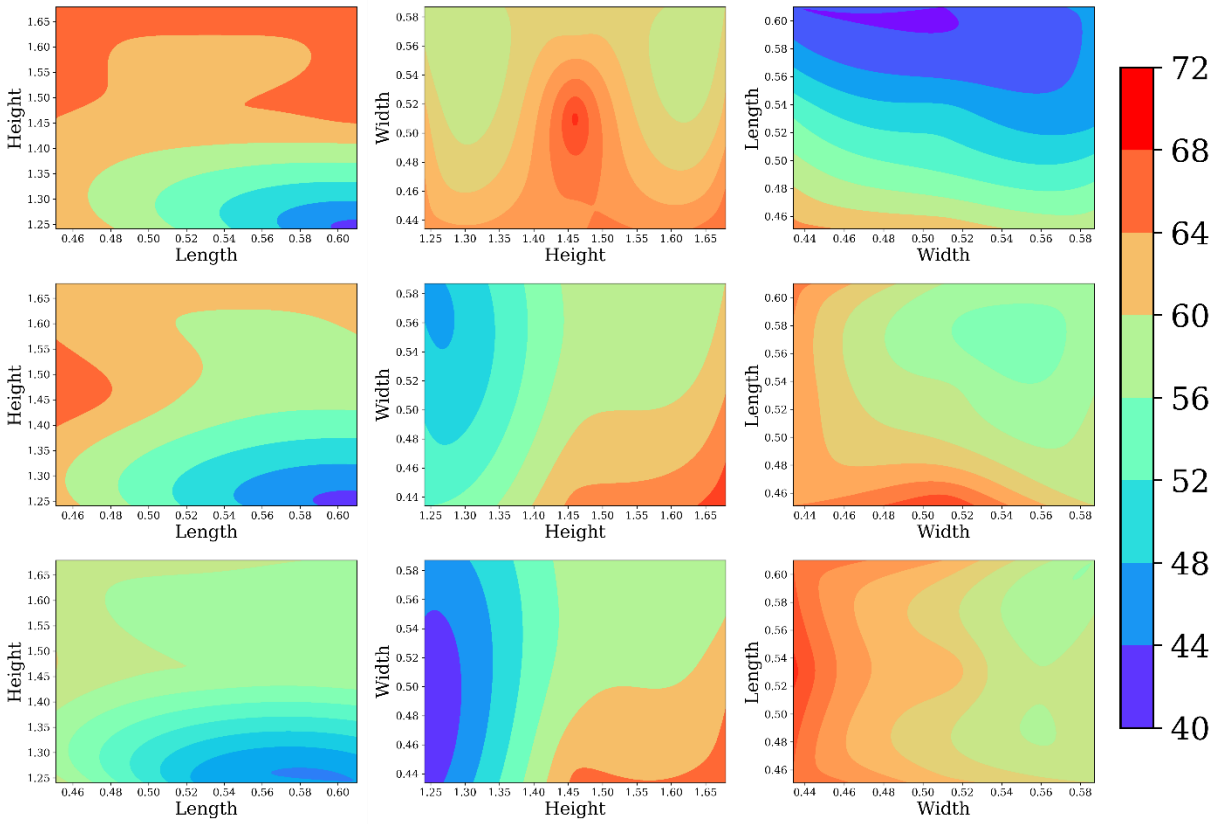

Figure 16: Display of the design table adjusting height, width, and length for their respective toughness output values in the aligned direction of the inner granular structure.

A similar trend holds true for the orthogonal loading direction (see Figure S1). Although, due to the flipped loading direction the parameters are flipped as well. In the case of the orthogonal loading direction, the height and width should be low. In addition, the thickness has a larger impact in the orthogonal direction, and a higher thickness leads to greater toughness parts. One thing to compare between these structures is the crack angle of failure. The more a crack

diverges from the straight path, the more energy is required to split the body, thus leading to a greater toughness. For the best-case structure, the crack angle was 35º from the vertical, whereas in the worst case the crack angle was 30º from the vertical. While this is not a huge difference, it stems from the geometry of the stiff and soft material redirecting the crack, which makes one better than the other.

The contour plots of Figure 16 and S1 show a high variation in the toughness of the materials within their respective design table of values. The lower toughness in the aligned direction is proposed to be due to the cross-sectional area of cell boundary that the material needs to break with respect to the amount of cell it needs to break. The ratio of cell boundary to cell in the plane perpendicular to the loading direction is much higher in the aligned direction than the orthogonal direction; this leads to a much stiffer structure, but also much less elongation. For this reason, the toughness in the aligned direction is far lower, but the strength is much higher as will be discussed in section 3.2.1.

3.1.2 Non-epitaxial cells

The non-epitaxial shape is a much more complex structure due to its formation at the meltpool boundaries. This structure is created when cells going towards the center of the first meltpool are remelted at the edge of a second meltpool. The new cells go towards the center of the second formed meltpool and thus these two cells have some angle between them depending on the geometry of the meltpools themselves. This leads to cells that can form with the same height, width, length, and thickness parameters, but also the angle between the cells can change, thus adding a fifth possible parameter.

The loading direction of these is less intuitive than the others, as these structures generally form on a track-track meltpool boundary which is approximately 45º to the build direction. To

quantify the characteristics of these shapes they are loaded pulling apart the meltpool (aligned) and pulling parallel to the meltpool (orthogonal). Since these structures have 5 parameters, running all simulations of these in a full factorial design table would take 273 experiments per orientation. In order to reduce unnecessary computation, a sensitivity analysis was performed for the basic influence of each parameter on strength and toughness. In the aligned direction, the height, thickness, and theta were shown to strongly influence strength and toughness. In the orthogonal direction, the width, length, thickness, and theta were shown to have an influence. For this reason, the simulations were run with the influential parameters changing and the others held constant. One thing to note is the smaller seed size required for mesh convergence for the non-epitaxial simulations as a whole in comparison to the inner granular and epitaxial cases (see Table 2). Due to the computational requirement for these simulations being much larger, the non-impactful parameters were held at the low value rather than the median value for these simulations.

In the aligned direction, the height and theta had a strong influence on the toughness of the structure as a whole. As shown in Figure 17, low height and high theta (measured perpendicular to the meltpool as shown in Figure 13) leads to a high toughness structure. The reasoning behind these parameters having a strong influence is more complex, but is likely based on the load path. As with any multi-material system, load is taken more by the stiff material than the soft material. For this reason, if the stiff material has a longer load path for a given shape width, e.g. by curving the stiff material within a soft matrix, this leads to a greater ability to stretch and straighten that material before it breaks. In addition, a higher curvature means the crack is likely to be diverted along an increased path length around or through this feature. The cell boundary of a non-epitaxial cell has a “curve” of stiff material that can be seen along the upper edge of each

cell. A low height leads to a smaller radius curve for a given angular fraction of a circle, and an increased theta leads to a higher angular fraction of the curve. In combination, these lead to a higher-curvature, stiffer material that can absorb more energy through straightening out as it fails, and divert the crack at a higher angle. These parametric adjustments can be seen in Figure 17. While thickness was tested for this system, it has little impact on the height and theta values.

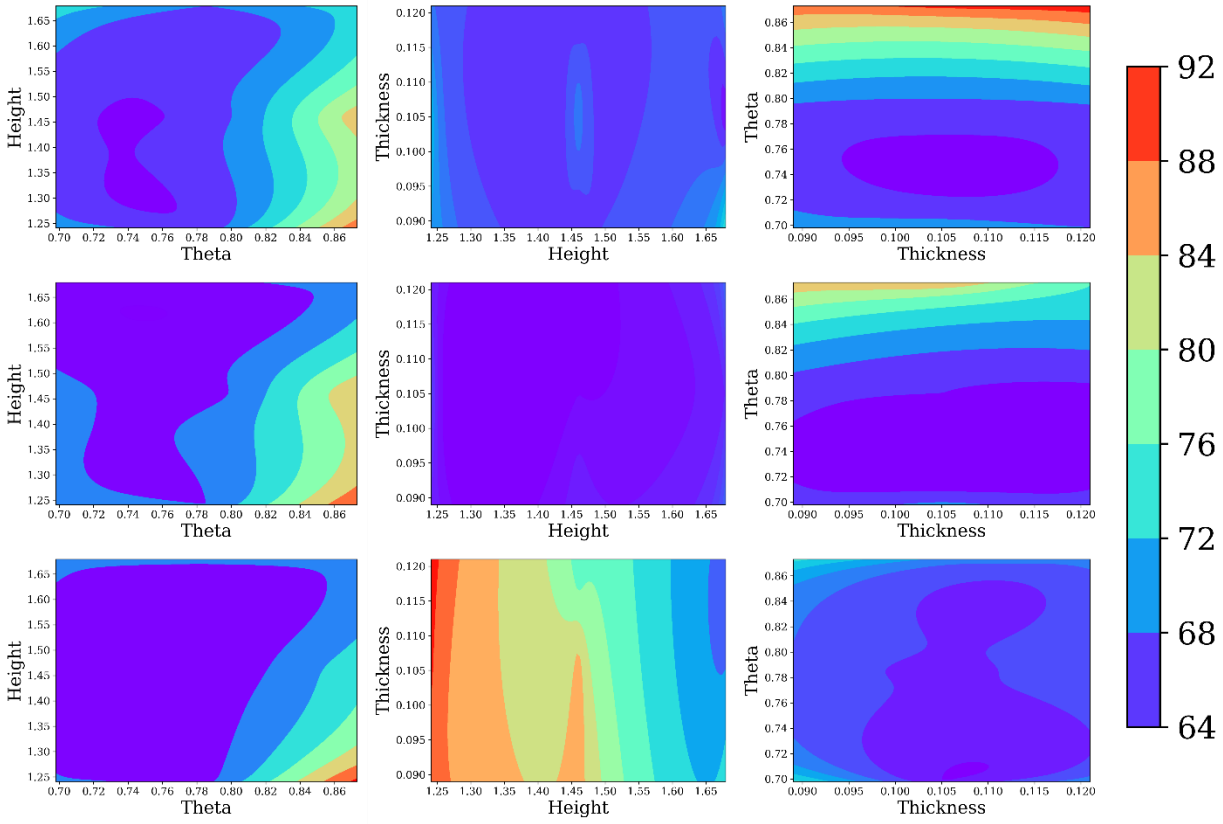

Figure 17: Display of the design table adjusting height, theta, and thickness for their respective toughness output values in the aligned direction of the non-epitaxial structure.

For the orthogonal direction, the structure is pulled parallel to the local meltpool. As this structure is now being pulled at orthogonally to the prior section, the parameters that influence it are different. In the orthogonal loading direction, the width, thickness, and theta all want to be

low in comparison to the height and length. This gives a structure as shown in Figure 15 that has relatively thin cells with high overlap from side to side. Essentially the load path through the cell boundary is a zig-zag shape along both sides of the non-epitaxial cell. This leads to a tough structure which can handle high elongation for the same reason as the aligned structure: the high angles within the load path mean energy is absorbed when the structure is straightened out, while also diverting the crack path. For the minimum toughness case, we see a nearly straight load path along both edges of the center cells in comparison to the maximum toughness case structure which has zig-zagged cell boundaries. These parameters and their impacts are shown in Figure S2. The trend of low thickness, theta, and width may seem a bit odd, as the ratio between the parameters is what matters, but in this case, the width, thickness, and theta values are compared to the height and length in addition to themselves.

3.1.3 Epitaxial Cells

Epitaxial cells are another cross-meltpool structure; however, rather than forming on the track-track boundaries these form on the layer-layer boundaries. In this case, a cell on the lower layer generally points upwards in the build direction, and the new layer forms atop the older layer. A new cell solidifies across the boundary and a high aspect ratio hexagon forms across the boundary. These cells have a very high height, and only slightly larger length and width than the inner granular cells. Due to the epitaxial cells' high aspect ratio, the structure essentially becomes a fibrous matrix composite, where increasing thickness and decreasing width directly increase the volume fraction of stiff material. With that in mind, those values are much more impactful on strength, and within the standard design space of these structures has so little variation in the load path that the impact on toughness is essentially entirely due to variation in the simulation itself. The range of toughness values seen in this simulation is only 10.5 MJ/m^3,

whereas the next lowest range is 23 MJ/m^3, with the highest range at 48 MJ/m^3. The other samples all show a large variation, as the structure as a design space that allows it to noticeably change the load path. The epitaxial cells, when pulled in the aligned direction, cannot form such that there is a substantial impact on toughness based on the formation geometry. The contour plot of length, width, and thickness are shown in Figure 18, the graphs of which show no meaningful correlation between the parameters studied and the toughness value.

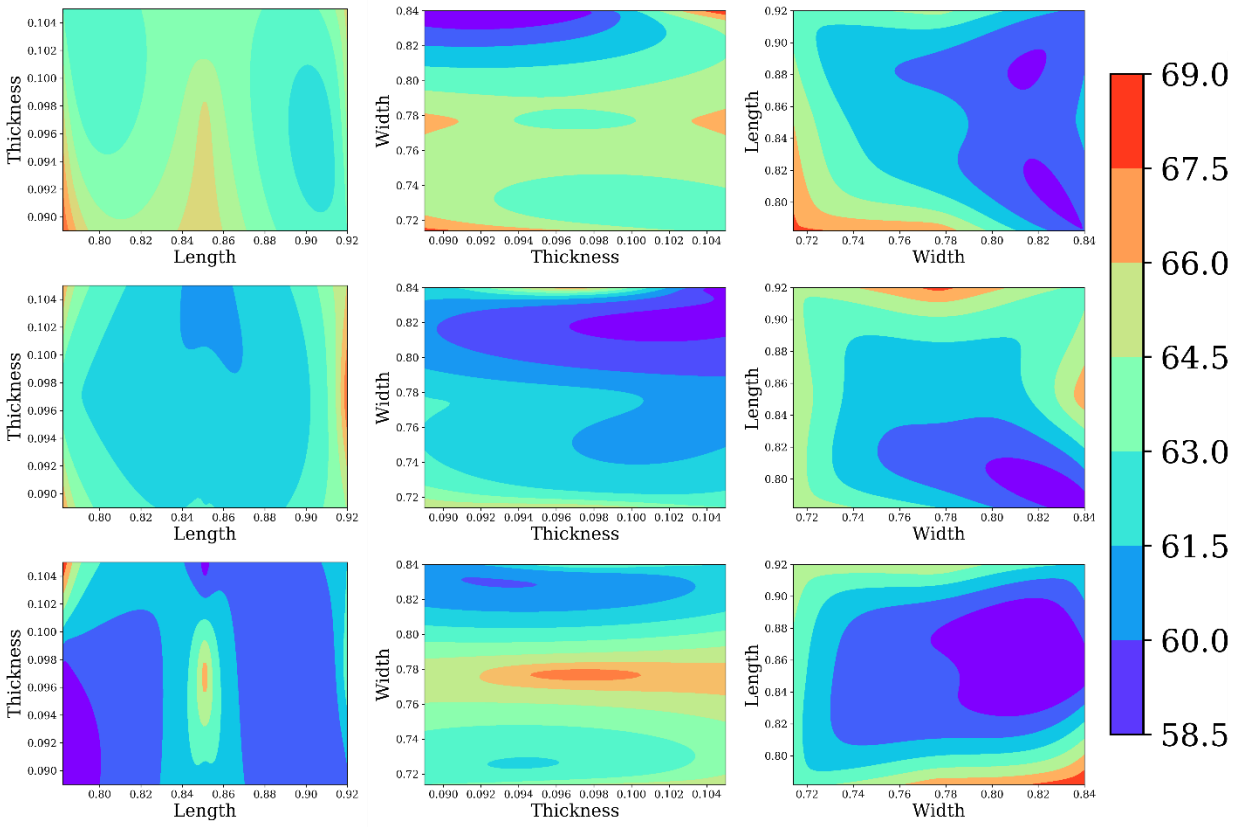

Figure 18: Display of the design table adjusting width, length, and thickness for their respective toughness output values in the aligned direction of the epitaxial structure.

For the orthogonal loading direction, there is slightly more geometric influence than the aligned direction, but it is still relatively low when compared with inner granular and non-epitaxial

directions (see Figure S3). In this loading case, there is a strong correlation between width, length, and toughness. This is similar to the inner granular direction, where a high width and low length is better. This higher width and low length means the crack needs to go more parallel to the loading direction, thus taking more energy to break the structure. Due to the high aspect ratio of the epitaxial cells, little impact from the other parameters is present.

3.2 Maximum Strength Characterization

The structures and geometric parameters we vary in this simulation have a high influence on many of the bulk material properties, including the maximum strength. This may seem like an odd value when one considers that these structures are created with two material both of which have strengths that were defined as parameters in the input. What we measure here is not the local strength, but rather the average strength of the entire structure, in other words, the maximum force the simulation reaches divided by the area of the simulation block. The change in strength is a result of the geometric arrangement in the microstructure. This value varies widely between different parameters and structures similar to toughness. In most cases, the maximum strength of a body can be achieved when the body has a straight load path, where many of the stiff material sections are loaded evenly and directly parallel to the loading direction. In every single case, the thickness was shown to have a correlation to strength, as the more thickness to the stiff section there is, the higher volume fraction each body is of the strong material thus increasing the bulk strength. This is mentioned within the specific sections below, but for this reason, the thickness is not plotted unless there are fewer than 2 other high-influence parameters.

3.2.1 Inner granular cells

The inner granular structure has a relatively high variation from the minimum to maximum strength based on the high change in the geometry of the body. Trends of changing the strength

as a function of the geometric features in the inner granular cells are shown in Figure 19, with the thickness plotted as the median value. As mentioned before, the highest load can be taken with straight parallel lines of stiff material, and the higher the ratio of stiff material to soft, the better. For the aligned direction, a low height and width and high length and thickness are desired for the best strength structures. The resultant shape of those parameters is repeated diamonds, where the cell boundaries are unbroken in long straight lines from one side of the body to the other. The high thickness means an increased volume fraction of the structure is a high strength material, thus leading to overall increased strength.

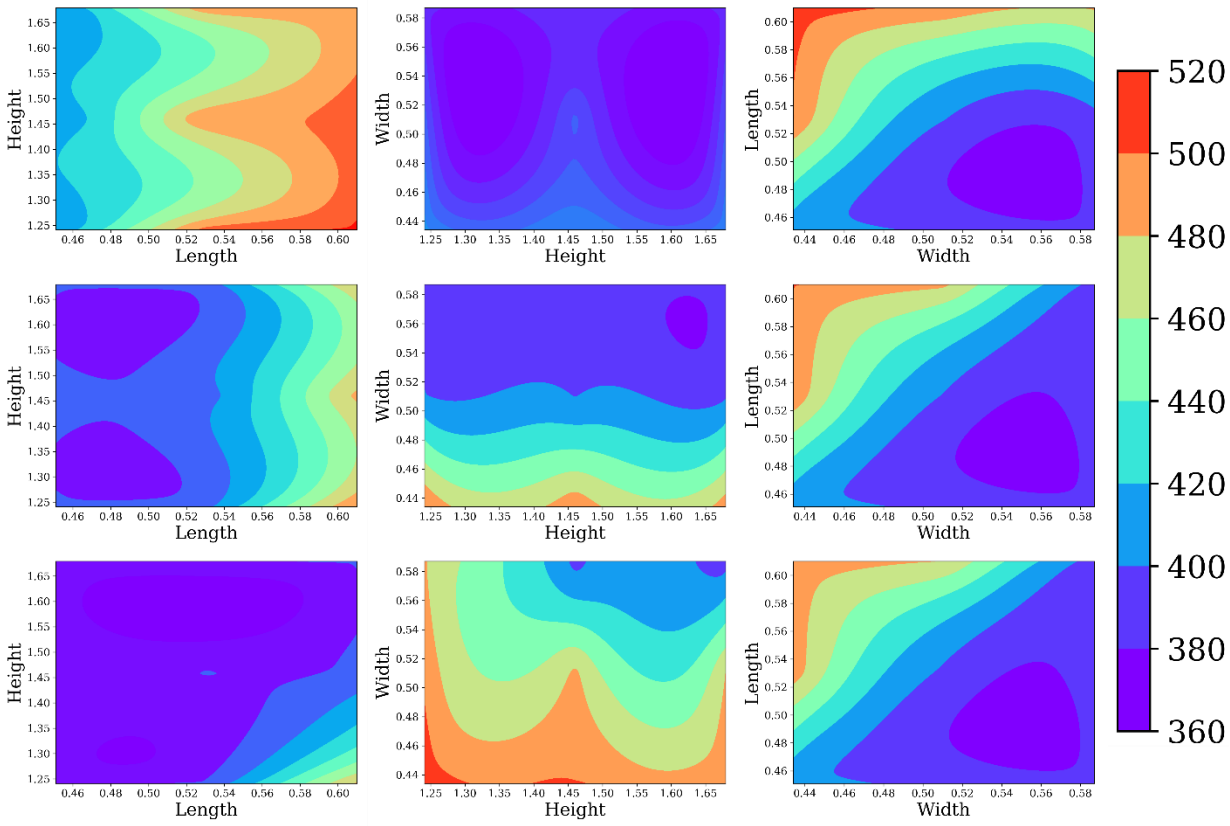

Figure 19: Display of the design table adjusting height, width, and length for their respective strength output values in the aligned direction of the inner granular structure.

In the orthogonal direction once again, all parameters were shown to have an impact on the strength, with a high height, low width, high length, and high thickness desired, with height and width having the greatest impact (see Figure S4). These structures overall should be long and thin, with thick cell boundaries for maximum strength. Both the width and the thickness influence the volume fraction of the stiff material, therefore increasing the volume fraction means the part can achieve a higher strength. In situations like this one, where design space does not allow the structure to form straight wide bands of solid material, the next best approach is increasing the amount of the stiff material as we see in Figure S4.

3.2.2 Non-Epitaxial

For the non-epitaxial cells in the aligned direction, thickness and theta have the strongest influence on the maximum strength of the structure. The change of strength as a function of these three major geometric parameters is shown in Figure 20. This structure, in the aligned direction, has a curved load path from one side to the other but is unbroken. The curvature of this load path is directly influenced by theta, with a lower theta meaning a straighter load path, thus a higher maximum load capability. As with the other structures, a higher load can be withstood with more stiff material, and thus a greater thickness results in increased load capacity.

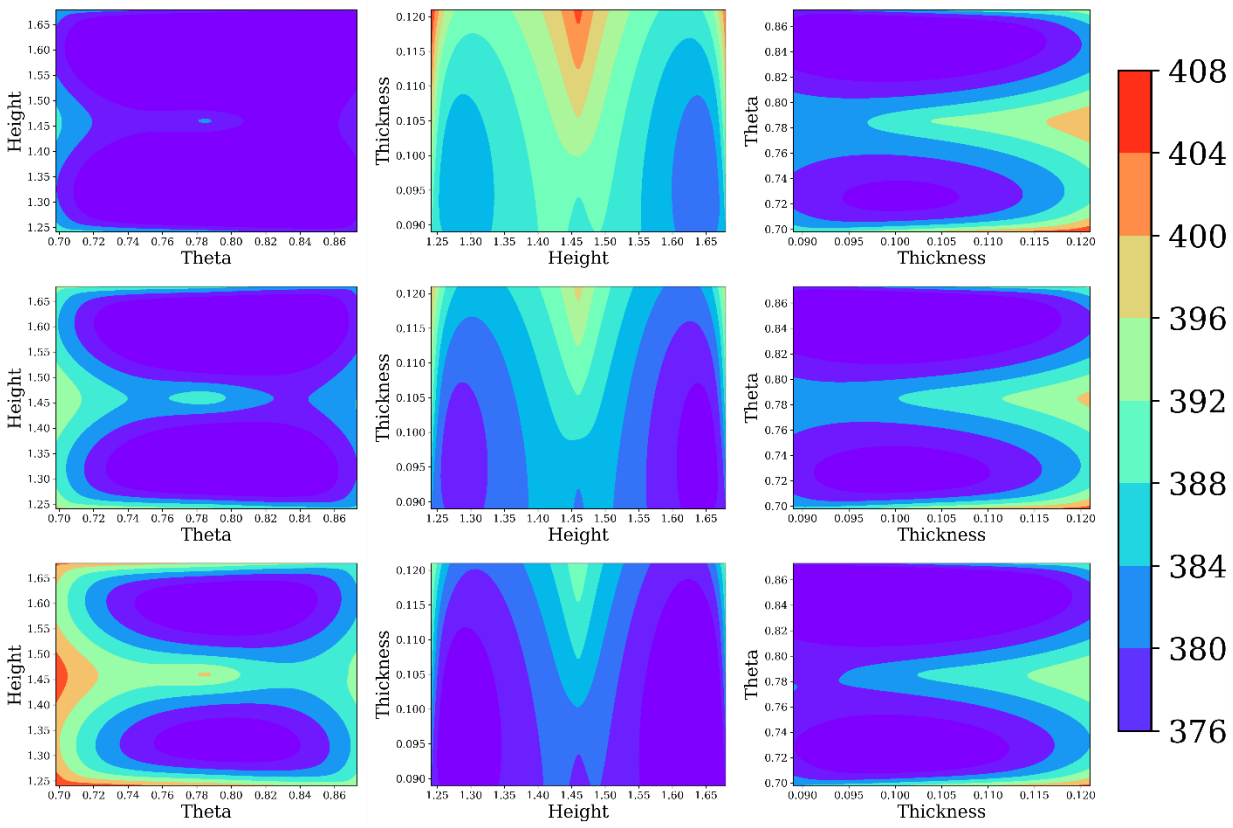

Figure 20: Display of the design table adjusting height, theta, and thickness for their respective strength output values in the aligned direction of the non-epitaxial structure.

For the orthogonal loading direction (see Figure S5), the same philosophy as in the aligned direction holds true, but in this case, the main two load paths are either side of the central column of non-epitaxial cells. For this reason, as little overlap as possible between the non-epitaxial cells in the central column and the normal cells on either side is ideal. To achieve this geometrically, high theta and thickness are desired. In addition, the point of the cells should be as small as possible, and it is beneficial to minimize the length.

3.2.3 Epitaxial

These structures are high aspect ratio hexagons where the cell boundary is reminiscent of stiff fibers in a composite. The geometry of these structures doesn't change drastically over their

design space, therefore the failure method remains the same across all parameters. This leads the strength to be optimal at high thickness and low width in order to maximize the volume fraction. While this is a relatively simple relationship, it holds true for the data shown in Figure 21.

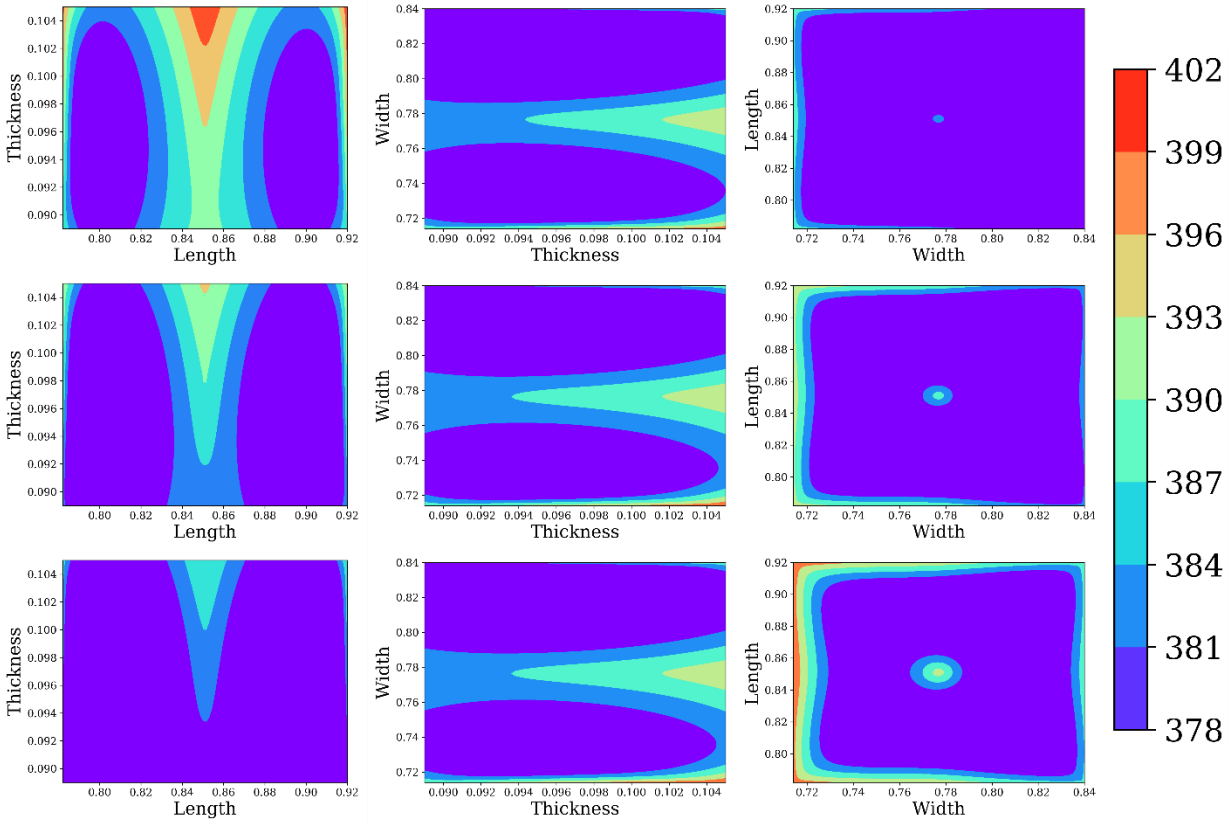

Figure 21: Display of the design table adjusting width, length, and thickness for their respective strength output values in the aligned direction of the epitaxial structure.

In the orthogonal direction, relatively low variation is present similar to the epitaxial toughness. In this case, however, there is a correlation between the length, width, and strength (Figure S6). A high length and low width is desired in order to achieve the highest strength structures. The reasoning for these parameters is the same as the inner granular reasoning, where the volume fraction of the stiff material is strongly correlated to the strength of the structure. Increasing this volume as much as possible leads to the highest overall strength part, as shown in Figure S6.

3.3 Variation of the measured parameters

In each of the structures (inner granular, non-epitaxial, and epitaxial), as parameters were changed, the toughness and strength were measured in both loading directions. These values can not only be compared among the different parameters for a given loading condition as in the sections above but can also be compared among the different load cases and structures in order to determine which structures are the most damage resistant or strong. The results of these values are all compared numerically and with data bars in Table 3.

Table 3: Comparative table showing the strength and toughness of each load and direction for the minimum and maximum values of parameterization, as well as the nominal condition.

		Inner Granular		Epitaxial		Non-Epitaxial	
		Aligned	Orthogonal	Aligned	Orthogonal	Aligned	Orthogonal
Strength (Mpa)	Maxima	520	375	402	375	408	392
	Nominal	399	271	395	286	395	375
	Minima	360	255	378	270	376	360
Toughness (MJ/m³)	Maxima	72	126	69	147	92	85
	Nominal	59	105	63	135	66	67
	Minima	40	78	58.5	123	64	45

3.3.1 Toughness Comparison

The toughness of these structures varies over a large range, from 40 – 147 MJ/m^3. For the inner granular and the epitaxial structures, the orthogonal loading direction sees a much higher toughness than the aligned direction. This makes sense and fits with reality as a much higher toughness is seen in plane than in the build direction for 3D printed metals [28]. The range these values occur over is quite large, meaning pure geometric changes to the same alloy at a micro-scale could lead to large improvements, especially as compared to the nominal values these were measured at. The non-epitaxial structures show a unique feature, which is that pulling in the aligned direction and the orthogonal direction have relatively similar toughnesses. This is

beneficial, as these structures are very difficult to isolate to a single loading direction as the non-epitaxial structures occur on a variety of angles with respect to the build direction due to their formation method.

These structures' nominal condition is below the maxima for every condition analyzed. In the inner granular case, the toughness can be improved by 21% on average, for the epitaxial case, the improvement is 9% on average, and lastly, for the non-epitaxial case, the improvement is 33% on average. This comparison shows that on average, these structures could be improved by 21% toughness solely based on geometry. With that in mind, some of these values are tradeoffs, such as the inner granular case where for the aligned direction a high height and low width improves the toughness, but for the orthogonal direction, a low height and high width improves the toughness. This allows the structure to be optimized for the loading condition that its part will be placed in, i.e. if the part will be loaded in tension in the planar direction, rather than the aligned direction the orthogonal loading direction toughness could be improved.

3.3.2 Strength Comparison

The strength of these materials ranges from 255 to 520 MPa. The pattern the strength follows is opposed to the toughness as shown in Figure 15 and Table 3, the inner granular and epitaxial cells see a much higher strength in the aligned case and a much lower strength in the orthogonal direction. The trade-off between optimizing the aligned and orthogonal directions still exists in this case and is described for each parameter in the sections above. The average improvement for all structures and loading directions is 18%. The inner granular structure can be improved on average 34%, the epitaxial structure 16%, and the non-epitaxial structure 4%.

4 Conclusions

In this work, we have shown the dependence of toughness and strength on geometry for inner granular, epitaxial, and non-epitaxial cells in 3D printed metals. This analysis was performed through representative stiff and soft materials in finite element modeling simulations. Based on these results, designers can optimize these structures for their specific load cases and application in order to get more efficient use out of a given material, thus increasing performance without the trade-off of increased weight. Generally, there exists an inverse correlation between these structures' strength and their toughness, especially true of the inner granular and epitaxial cases. Through this optimization within a roughly 15% adjustment around the average cell, we show that it is possible to gain up to 21% toughness and 18% strength for our design space.

References:

1. Yadroitsev, I., et al., *Energy input effect on morphology and microstructure of selective laser melting single track from metallic powder.* Journal of Materials Processing Technology, 2013. **213**(4): p. 606-613.

2. Wei, Y.J., et al., *Evading the strength- ductility trade-off dilemma in steel through gradient hierarchical nanotwins.* Nature Communications, 2014. **5**: p. 8.

3. Tucho, W.M., et al., *Investigation of effects of process parameters on microstructure and hardness of SLM manufactured SS316L.* Journal of Alloys and Compounds, 2018. **740**: p. 910-925.

4. Sun, Z.J., et al., *Simultaneously enhanced strength and ductility for 3D-printed stainless steel 316L by selective laser melting.* Npg Asia Materials, 2018. **10**: p. 10.

5. Song, B., et al., *Differences in microstructure and properties between selective laser melting and traditional manufacturing for fabrication of metal parts: A review.* Frontiers of Mechanical Engineering, 2015. **10**(2): p. 111-125.

6. Shrestha, S., S. Rauniyar, and K. Chou, *Thermo-Fluid Modeling of Selective Laser Melting: Single-Track Formation Incorporating Metallic Powder.* Journal of Materials Engineering and Performance, 2019. **28**(2): p. 611-619.

7. Saeidi, K., et al., *Austenitic stainless steel strengthened by the in situ formation of oxide nanoinclusions.* Rsc Advances, 2015. **5**(27): p. 20747-20750.

8. Saeidi, K. and F. Akhtar, *Subgrain-controlled grain growth in the laser-melted 316 L promoting strength at high temperatures.* Royal Society Open Science, 2018. **5**(5): p. 7.

9. Liverani, E., et al., *Effect of selective laser melting (SLM) process parameters on microstructure and mechanical properties of 316L austenitic stainless steel.* Journal of Materials Processing Technology, 2017. **249**: p. 255-263.

10. Jung, H.Y., et al., *Fabrication of Fe-based bulk metallic glass by selective laser melting: A parameter study.* Materials & Design, 2015. **86**: p. 703-708.

11. Taylor, S.L., et al., *Iron and Nickel Cellular Structures by Sintering of 3D-Printed Oxide or Metallic Particle Inks.* Advanced Engineering Materials, 2017. **19**(11): p. 8.

12. Libonati, F., et al., *Bone-Inspired Materials by Design: Toughness Amplification Observed Using 3D Printing and Testing.* Advanced Engineering Materials, 2016. **18**(8): p. 1354-1363.

13. Dadbakhsh, S., et al., *Effect of SLM Parameters on Transformation Temperatures of Shape Memory Nickel Titanium Parts.* Advanced Engineering Materials, 2014. **16**(9): p. 1140-1146.

14. Lewandowski, J.J. and M. Seifi, *Metal Additive Manufacturing: A Review of Mechanical Properties*, in *Annual Review of Materials Research, Vol 46*, D.R. Clarke, Editor. 2016, Annual Reviews: Palo Alto. p. 151-186.

15. Ahmadi, A., et al., *Effect of manufacturing parameters on mechanical properties of 316L stainless steel parts fabricated by selective laser melting: A computational framework.* Materials & Design, 2016. **112**: p. 328-338.

16. Choi, J.P., et al., *Densification Behavior of 316L Stainless Steel Parts Fabricated by Selective Laser Melting by Variation in Laser Energy Density.* Materials Transactions, 2016. **57**(11): p. 1952-1959.

17. Farshidianfar, M.H., A. Khajepour, and A.P. Gerlich, *Effect of real-time cooling rate on microstructure in Laser Additive Manufacturing.* Journal of Materials Processing Technology, 2016. **231**: p. 468-478.

18. Kunze, K., et al., *Texture, anisotropy in microstructure and mechanical properties of IN738LC alloy processed by selective laser melting (SLM).* Materials Science and Engineering a-Structural Materials Properties Microstructure and Processing, 2015. **620**: p. 213-222.

19. Wang, Y.M., et al., *Additively manufactured hierarchical stainless steels with high strength and ductility.* Nature Materials, 2018. **17**(1): p. 63-+.

20. Rannar, L.E., et al., *Hierarchical structures of stainless steel 316L manufactured by Electron Beam Melting.* Additive Manufacturing, 2017. **17**: p. 106-112.

21. Zhong, Y., et al., *Intragranular cellular segregation network structure strengthening 316L stainless steel prepared by selective laser melting.* Journal of Nuclear Materials, 2016. **470**: p. 170-178.

22. Yasa, E. and J.P. Kruth, *Microstructural investigation of Selective Laser Melting 316L stainless steel parts exposed to laser re-melting*, in *1st Cirp Conference on Surface Integrity*, E. Brinksmeier, I.S. Jawahir, and D. Meyer, Editors. 2011, Elsevier Science Bv: Amsterdam.

23. Saeidi, K., et al., *Hardened austenite steel with columnar sub-grain structure formed by laser melting.* Materials Science and Engineering a-Structural Materials Properties Microstructure and Processing, 2015. **625**: p. 221-229.

24. Prashanth, K.G. and J. Eckert, *Formation of metastable cellular microstructures in selective laser melted alloys.* Journal of Alloys and Compounds, 2017. **707**: p. 27-34.

25. Saeidi, K., et al., *Transformation of austenite to duplex austenite-ferrite assembly in annealed stainless steel 316L consolidated by laser melting.* Journal of Alloys and Compounds, 2015. **633**: p. 463-469.

26. Jiang, W.G., et al., *Homogenized Finite Element Analysis on Effective Elastoplastic Mechanical Behaviors of Composite with Imperfect Interfaces.* International Journal of Molecular Sciences, 2014. **15**(12): p. 23389-23407.

27. Mirzaeifar, R., et al., *Defect-Tolerant Bioinspired Hierarchical Composites: Simulation and Experiment.* Acs Biomaterials Science & Engineering, 2015. **1**(5): p. 295-304.

28. Gu, D.D. and H.Y. Chen, *Selective laser melting of high strength and toughness stainless steel parts: The roles of laser hatch style and part placement strategy.* Materials Science and Engineering a-Structural Materials Properties Microstructure and Processing, 2018. **725**: p. 419-427.

Supplementary Material:

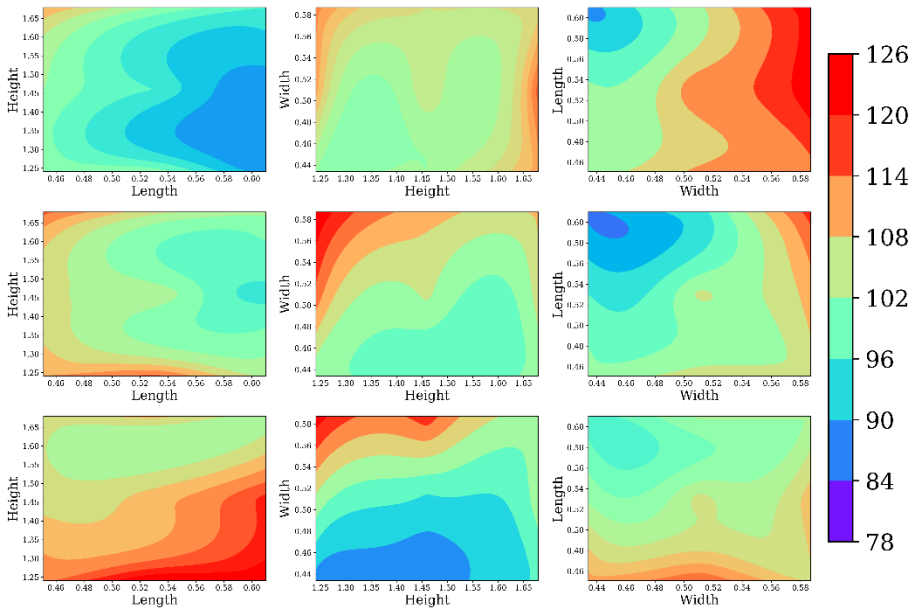

Figure S22: Display of the design table adjusting height, width, and length for their respective toughness output values in the orthogonal direction of the inner granular structure.

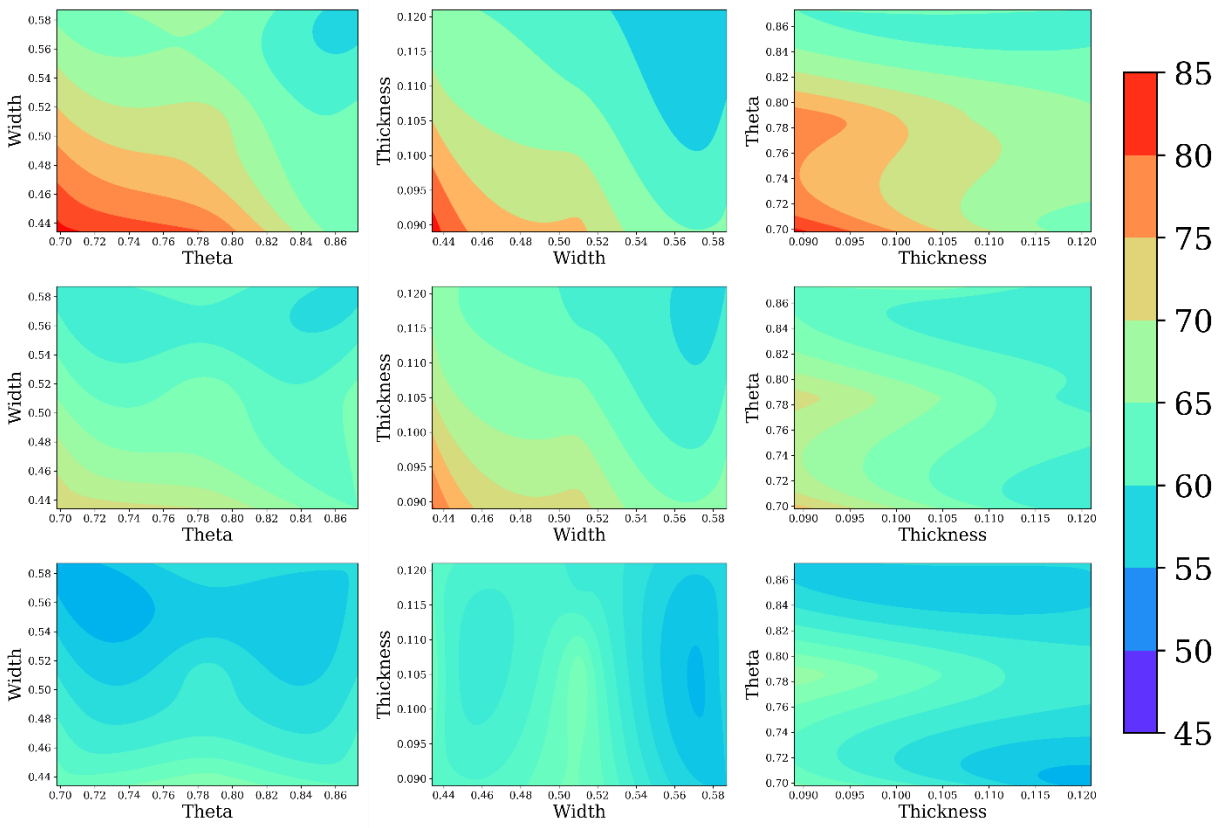

Figure S23: Display of the design table adjusting width, theta, and thickness for their respective toughness output values in the orthogonal direction of the non-epitaxial structure.

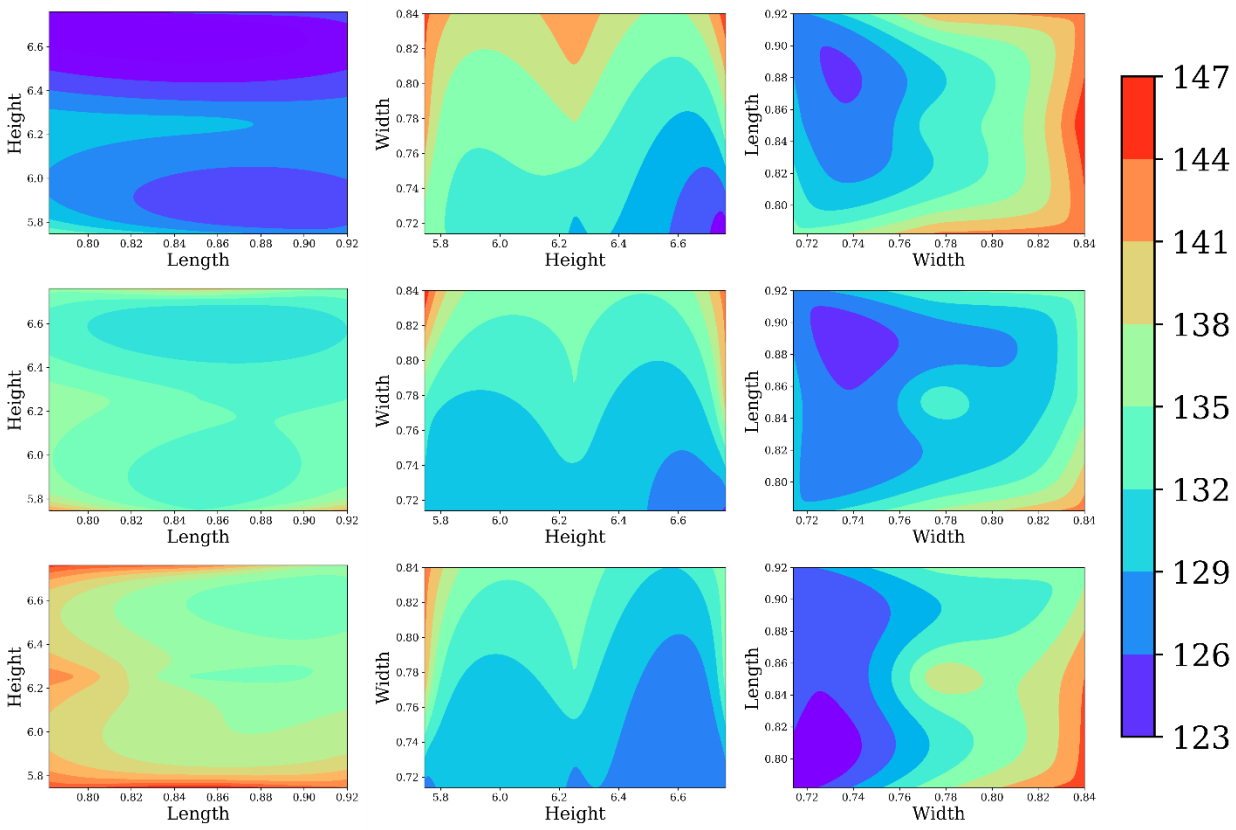

Figure S24: Display of the design table adjusting height, width, and length for their respective toughness output values in the orthogonal direction of the epitaxial structure

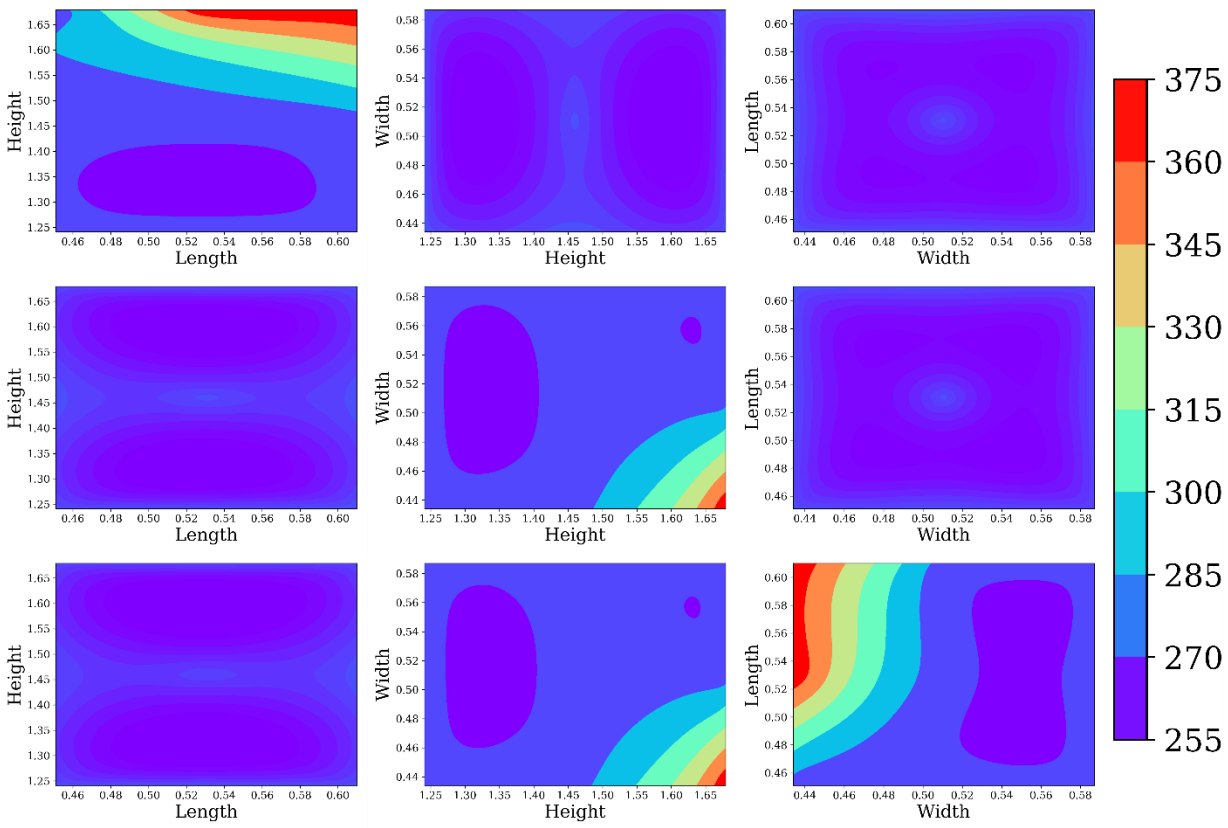

Figure S25: Display of the design table adjusting height, width, and length for their respective strength output values in the orthogonal direction of the inner granular structure

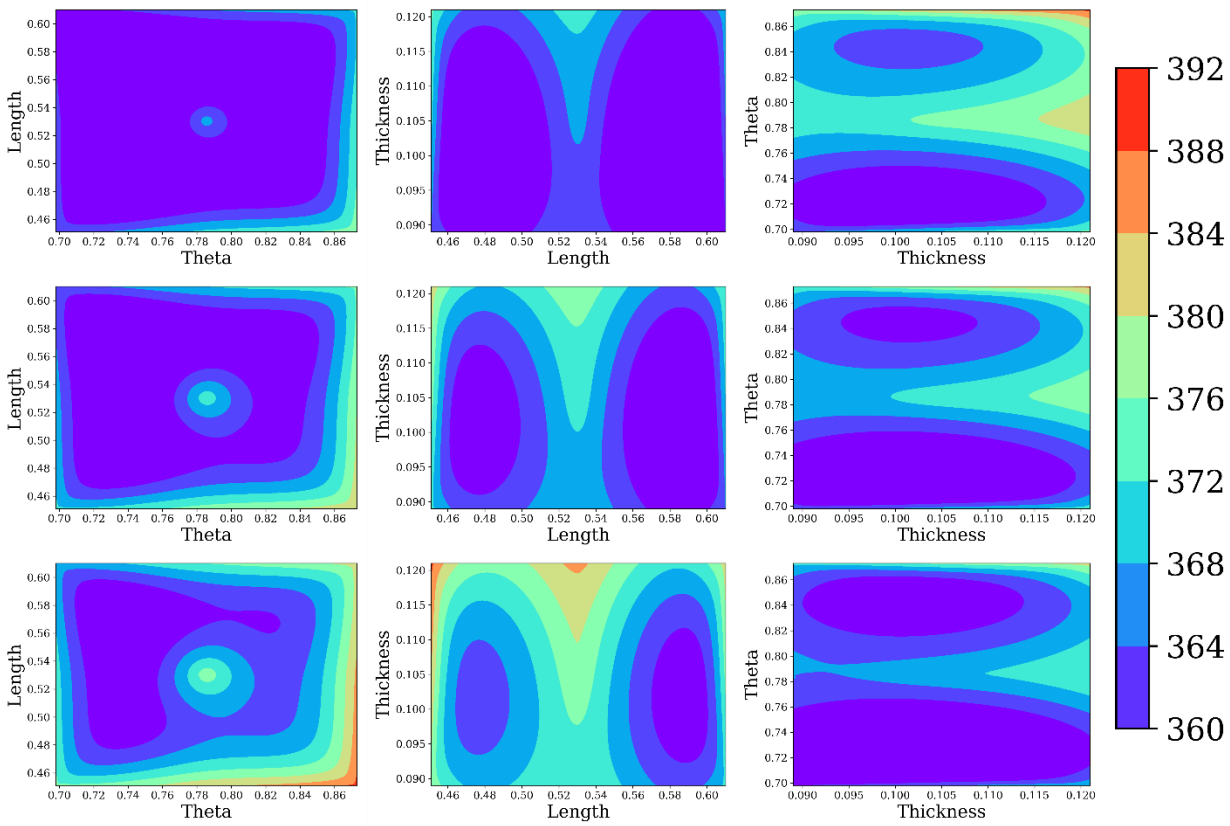

Figure S26: Display of the design table adjusting length, theta, and thickness for their respective strength output values in the orthogonal direction of the non-epitaxial structure

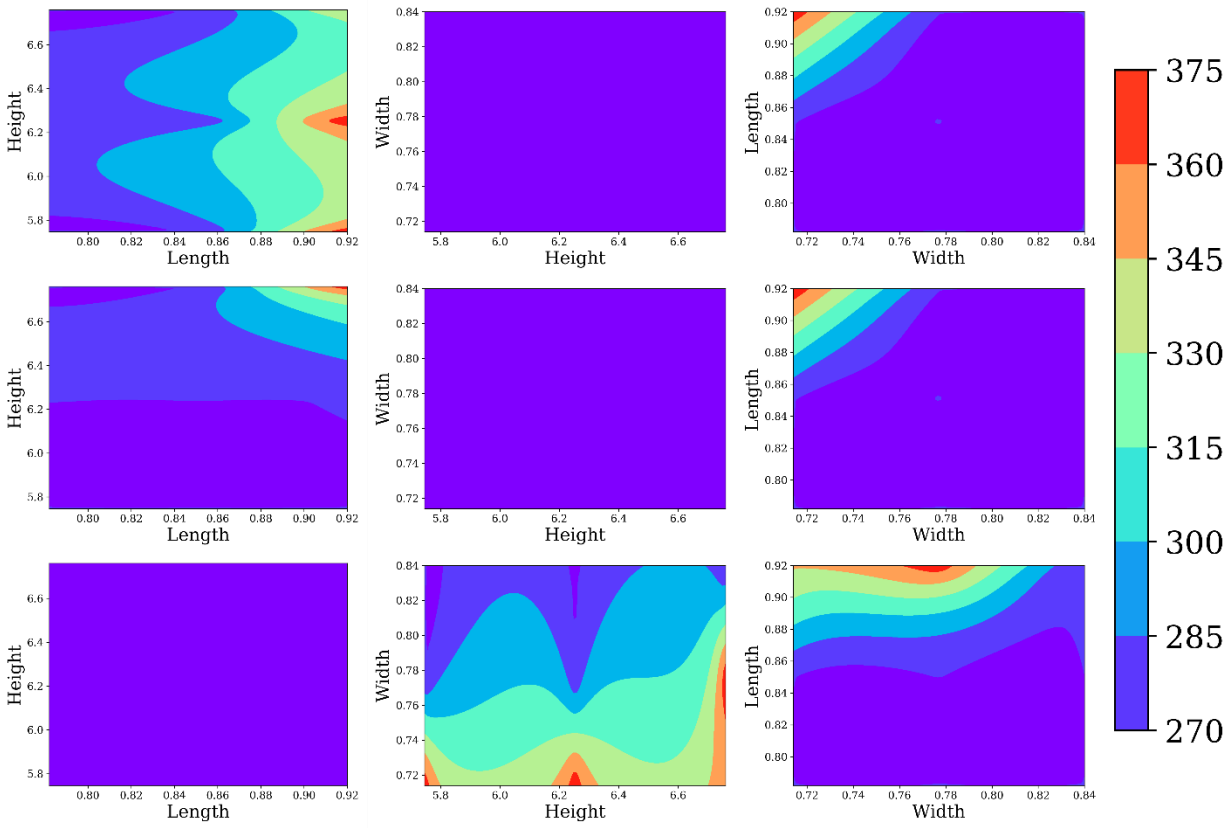

Figure S27: Display of the design table adjusting width, length, and height for their respective strength output values in the orthogonal direction of the epitaxial structure

Conclusions and Future work

1 Contributions to the Field

The work presented in this thesis contains many methods, results, and conclusions that are novel work, contributing new knowledge to the 3D fabrication field. From a methodology standpoint, there were three main accomplishments. Firstly, using a neural network to differentiate microstructure (cells from cell boundaries in this case) from SEM images. This allows the second novel method to exist which is the automatic creation of a finite element model based on the differentiated image. This custom program allows Abaqus to interface with a given image such that it creates a model with one model for the cells and one for the cell boundaries, and then defines the elements in the model based on the image it read to recreate the geometry from SEM. Lastly, we used a 3D multi-material printer in order to recreate our sample geometry with a stiff and soft material distribution. This sample was used to analyze the fracture and failure mechanics of this geometry, in addition to studying the stress delocalization of the stress concentration at a crack-tip.

From a results and conclusions standpoint, there are three main novel works. Showing how the crack concentration is delocalized at a crack-tip with respect to a solid phase material due to the hierarchical material distribution is novel. Secondarily, showing the strain field across a given SLM part at the scale of cells and meltpools both computationally through finite element modeling, and experimentally through the multi-material prints. These experiments and simulations show that the SLM part will have an increased damage tolerance with respect to a single-phase material. Lastly, we show that through adjustment of the shape and size of the cells' shape better bulk material properties can be achieved, including higher maximum strength or higher toughness.

2 Assumptions and limitations

In any work that involves experimentation or simulation, certain assumptions need to be made in order to make the work feasible to complete and perform. The aim of this section is to outline the assumptions that were made throughout my work, and explain how this impacts the results and influences the conclusions. For clarity, these will be explained and quantified in the order that the conclusions were presented.

For the neural network method, there are two main limitations of this work. Firstly, this method relies on the original masks that were used to train the neural network being correct and accurate. As these have to be hand created, this means that the model is limited by the creator of the masks' accuracy. Secondarily, assuming this model appropriately represents the geometry, the thickness of the cell boundaries is an approximation. This approximation is based on two things: what the neural network "sees" the cell boundary to be, but also this value can be checked or compared to the total volume fraction of cell boundary in the masks of similar cell types. By this logic, the cell boundaries could be thickened or thinned in order to get a correct overall volume fraction or average cell boundary thickness, but the localized cell boundary thickness may not be perfectly correct.

The creation of the model itself is accurate, but the model has limitations; the cell boundary material is the largest limitation of this section. This work assumes the cell boundaries are stiffer and stronger based on their elemental composition, phase, and the dislocation content in these areas. Even with the current research on these topics, no one has proven the current material properties of the cell boundaries, thus this work and model only applies if the cell boundaries are a similar toughness material, which is stiffer and stronger than the cells. The amount difference will impact the actual numbers of how much toughness and strength loss each section and

sample sees, but the material will follow the same trend with the same failure mechanisms assuming these conditions.

The main drawbacks of the multi-material printing are similar to the modeling. The representative materials mean that the trend and failure mechanisms of the result will follow a similar pattern assuming the cell boundary material is a stiffer stronger material. The 3D printing also introduces the element of the bonding or interface between the two materials printed; in this case, the interfacial areas didn't fail, rather the cell boundaries then the cells themselves did so this wasn't a limitation in this study but could play a limitation in similar studies with different materials printed.

As for the results, the crack concentration and strain field studies are similarly dependent on the physical properties of the cell boundary. The results showing stress delocalization at the crack-tip, the way the strain field is distributed, and the respectively high damage tolerance compared to a single-phase material are all results of the cell boundary's increased strength and toughness versus the cell's properties. As this impacts all the cell/cell boundary studies this same limitation is applied to the optimization of the cellular shape as well.

3 Future Works

Some of these studies were conclusive in their own ways, but all of them can either be directly continued to increase the knowledge of the community or expanded in a parallel direction to a similar task that would benefit from them. The neural network which we used for cell and cell boundary differentiation could be applied to many other kinds of microstructure. From an SLM standpoint, this could be applied to both grains/grain boundaries, and meltpools / meltpool boundaries. We have taken this a step further for SLM parts and expanded our program to include EBSD mappings for use with crystal plasticity modeling such that grains, meltpools, and

cells can all be included within the same model from a single section of a real sample. This will expand the current work when these simulations are run to show how grains fit into the failure mechanisms of these bodies along with cells and cell boundaries. On a parallel path, this same kind of neural network could be applied to any material with a microstructure one wants to analyze that shows up as unique colors in SEM. For instance, precipitates, spinoidal decomposition, grain boundaries, meltpools, or even some composites. All of these can be split into sections based on visual appearance for different elements, alloys, or phases of material thus having different properties. Once these bodies are differentiated by this neural network, they can have models created automatically the same as was done in our study.

The multi-material printing approach can be applied to a similar set of works as the neural network. Any kind of microstructure that is challenging to study deformation mechanisms at the real scale can be scaled up and tested in a similar manner. This kind of testing all comes with the same limitation as the tests we ran, where the result is a qualitative result that shows the trend of style of failure based on a multi-material system, rather than the exact numerical solution based on correct materials.

As for the results, there are two main future works aside from the grains being included in the model. From the standpoint of experimental analysis on strain field and deformation mechanisms, our testing was done with representative materials that were scaled up. We tried to use surfactants and gold nano-particles as “species” for DIC on the real samples, but we could not get the density high enough. This test has the resolution to show grain size DIC or meltpool scale DIC, but not the influence of cell boundaries. For this work to continue, we would need to find a better speckling method, which has higher density, and smaller speckles to test the real samples with.

Another future work of the model is expanding the amount of simulations completed. Due to the computation time, only two simulations were run for each section studied, one with a pre-crack and one without. Taking a larger volume of the same kind of section (i.e. inner granular, epitaxial, non-epitaxial, or triple junction) and testing different areas of the whole body with these features would lead to a proper measure of variance and error in each of these sections. This could be done both experimentally and from a simulation standpoint. Currently, this wouldn't have a huge impact, as due to not knowing the real stiffness or strength of the cell boundary our numbers show a trend rather than true values for a real 316L system. With that in mind, once the real material properties of cell boundaries are known, this can be expanded to be perfectly accurate simulation, and with multiple simulations of each feature, one could get a distribution function of the toughness and strength loss for each feature.

The other result with a direct path future work was the optimization of the cell shapes. Now that we have shown that different cell shapes can lead to stronger and tougher bulk properties, the 3D fabrication community needs to find a method to finely control the geometry of these cells and boundaries, either based on elemental changes and fine control or based on laser parameters. Once the cell shapes can be controlled, then parts with higher strength or toughness in certain directions can be created, thus making a more ideal part for a given application.